Blade Displacement Measurement Technique Applied to a Full-Scale Rotor Test

Anita I. Abrego
Aerospace Engineer
Anita.I.Abrego@nasa.gov

Lawrence E. Olson
Aerospace Engineer
olawrence6@gmail.com

Ethan A. Romander
Aerospace Engineer
Ethan.A.Romander@nasa.gov

National Aeronautics and Space Administration
Ames Research Center
Moffett Field, CA

Danny A. Barrows
Aerospace Engineer
Danny.A.Barrows@nasa.gov

Alpheus W. Burner
Aerospace Engineer
Apheus.W.Burner@nasa.gov
Jacobs Technology

National Aeronautics and Space Administration
Langley Research Center
Hampton, VA

ABSTRACT

Blade displacement measurements using multi-camera photogrammetry were acquired during the full-scale wind tunnel test of the UH-60A Airloads rotor, conducted in the National Full-Scale Aerodynamics Complex 40- by 80-Foot Wind Tunnel. The objectives were to measure the blade displacement and deformation of the four rotor blades as they rotated through the entire rotor azimuth. These measurements are expected to provide a unique dataset to aid in the development and validation of rotorcraft prediction techniques. They are used to resolve the blade shape and position, including pitch, flap, lag and elastic deformation. Photogrammetric data encompass advance ratios from 0.15 to slowed rotor simulations of 1.0, thrust coefficient to rotor solidity ratios from 0.01 to 0.13, and rotor shaft angles from -10.0 to 8.0 degrees. An overview of the blade displacement measurement methodology and system development, descriptions of image processing, uncertainty considerations, preliminary results covering static and moderate advance ratio test conditions and future considerations are presented. Comparisons of experimental and computational results for a moderate advance ratio forward flight condition show good trend agreements, but also indicate significant mean discrepancies in lag and elastic twist. Blade displacement pitch measurements agree well with both the wind tunnel commanded and measured values.

NOTATION

c	blade chord, in
C_T	rotor thrust coefficient
C_Q	rotor torque coefficient
C_T/σ	ratio of thrust coefficient to rotor solidity
C_Q/σ	ratio of torque coefficient to rotor solidity
dx, dy, dz	computed displacement of quarter chord, normalized by rotor radius R
dxang, dyang, dzang	computed angular changes about X, Y, Z axes
xqc, yqc, zqc	quarter chord normalized coordinates to rotor radius
L	separation of leading and trailing edge targets, nominal, in
M_{tip}	blade tip Mach number
r	radial coordinate, in
R	rotor radius, 322 in
X	rotor coordinate system spanwise, in
Y	rotor coordinate system chordwise, in
Z	rotor coordinate system vertical, in
α_s	geometrical shaft angle, positive aft, deg
μ	advance ratio
ψ	rotor azimuth, deg
σ	rotor solidity, 0.0826

INTRODUCTION

In May 2010, a full-scale wind tunnel test of the UH-60A Airloads rotor was completed in the USAF National Full-Scale Aerodynamics Complex (NFAC) 40- by 80-Foot Wind Tunnel at NASA Ames Research Center (Ref. 1). The test was a joint venture between NASA and the U.S. Army to acquire an expanded database, supplementing the widely used and extensive 1993 UH-60A airloads flight test data (Ref. 2). Unique measurement techniques, such as blade displacement multi-camera photogrammetry, were implemented to expand the airloads database and assist with the validation of rotorcraft predictive tools.

Presented at the American Helicopter Society 68th Annual Forum, Fort Worth, Texas, May 1 – 3, 2012.

Blade displacement measurements are used to resolve rotor blade shape and position, including blade pitch, flap, lag and elastic deformations. When combined with blade airloads and wake measurements, a comprehensive dataset is formed that directly relates rotor performance to the physical properties of the flow. The accurate prediction of rotor blade rigid body motion and elastic displacements is a key goal in the development of improved rotorcraft design and analysis techniques. Furthermore, continued progress toward more tightly coupled multi-disciplinary, higher fidelity rotorcraft aeromechanics analysis techniques can be paced in part by the availability of detailed experimental measurements obtained under conditions representative of the actual flight environment.

Traditionally, blade displacements have been derived from strain gauges imbedded in the rotor blades. Due to blade size limitations and the limited availability of rotating instrumentation channels, the number of possible sensors is usually insufficient to fully resolve the blade motion. As an alternative, optical methods can be used to provide a description of the blade geometry over most of its length with the added benefit of reduced fabrication costs and sensor count (Ref. 3).

High-quality rotor blade displacement data sets are relatively rare. A Blade Deformation Measurement System using CCD cameras imbedded in the hub to measure blade movement and deformation of a Ka-25 helicopter blade was reported in 1997 (Ref. 4). In 2001 the Higher Harmonic Control Aeroacoustic Rotor Test (HART II) used Stereo Pattern Recognition to measure blade position and deflection of a 40% Mach scaled, 2-meter radius BO-105 model rotor (Ref. 5). This technique was based on a 3-dimensional reconstruction of visible marker locations using stereo photogrammetry, providing the blade motion parameters in flap, lag and torsion.

More recently, in preparation for the UH-60A Airloads wind tunnel test, rotor blade displacement measurements were acquired during two earlier wind tunnel tests in the NFAC 40- by 80-Foot Wind Tunnel. The blade displacement measurement system was briefly used in each of these two preliminary tests at increasing levels of complexity and development. The first, in 2008 during the Smart Material Actuated Rotor Technology (SMART) test and then in 2009 for the Individual Blade Control (IBC) test (Ref. 6). For each of the three wind tunnel test entries, the photogrammetry system progressively doubled in size and complexity. A single PC assembly with two-cameras was used for the SMART test, two PCs with four-cameras were used for the IBC test, and four PCs with eight-cameras were used for the final and much more extensive Airloads test. The final test included 27 sets of data for all four blades over the full rotor azimuth and many additional limited sets tracking one blade per quadrant. The measurement effort during the first two test entries, while brief, significantly influenced and improved the final system design for the detailed blade displacement measurements during the more comprehensive Airloads test.

The objective of this paper is to provide an overview of the blade displacement measurement methodology and system development. Also presented are descriptions of image processing, uncertainty considerations, preliminary results covering static and moderate advance ratio test conditions, and initial comparisons with computational results.

TEST DESCRIPTION

The test was conducted in the NFAC 40- by 80-Foot Wind Tunnel using a Sikorsky Aircraft UH-60A rotor system mounted on the NASA Large Rotor Test Apparatus (LRTA) as seen in Fig. 1. The closed test section consists of semicircular sides and closed-circuit air return passage that are lined with sound-absorbing material to reduce acoustic reflections. The test section dimensions are 39 feet high, 79 feet wide, and 80 feet long with a maximum test section velocity of approximately 300 knots. The LRTA, a special-purpose drive and support system designed to test helicopters and tilt rotors in the NFAC (Ref. 7), was mounted on three struts, allowing for an angle-of-attack range of +15° to -15°.

Figure 1. UH-60A Airloads rotor installed on the Large Rotor Test Apparatus (LRTA) in the NFAC 40- by 80-Foot Wind Tunnel.

The UH-60A is a four-bladed articulated rotor system consisting of a hub, blade pitch controls, bifilar vibration absorber, and main rotor blades. The blades used in this wind tunnel test were the same four rotor blades flown during the UH-60A Airloads Program (Ref. 2). Two blades were heavily instrumented, one with 242 dynamic pressure transducers (blade 1) and the other with a mix of strain-gages and accelerometers (blade 3). A summary of the rotor system parameters is provided in Table 1.

Although the UH-60A is classified as an articulated or hinged helicopter, there are no actual hinges at the blade root. Rather, the blade motions occur around elastomeric bearings and the "hinges" are the focal points of the

bearings. During both the flight and wind tunnel tests, measurements of the blade motions about these focal points were accomplished through a combination of RVDTs and links, referred to as the Blade Motion Hardware (BMH) or "crab arm." A crab arm is installed on each blade and provides measurements of the blade flap, lead-lag, and pitch angles.

A second blade motion measurement system composed of four sets of three laser distance transducers (one set mounted to each hub arm) as described in Ref. 1, was also used. The calibration of both systems was performed simultaneously in the wind tunnel.

Table 1. UH-60A Rotor Parameters (Ref. 7)

Parameter	Value
Number of blades	4
Radius, in	322
Nominal chord, in	20.76
Equivalent blade twist, deg	-18
Blade tip sweep, deg aft	20
Geometric solidity ratio	.0826
Airfoil section designation	SC1095/SC1094R8
Thickness, % chord	9.5
100% RPM	258

Test Conditions

The primary wind tunnel test data were acquired during speed sweeps at 1-g simulated flight conditions up to an advance ratio of $\mu = 0.4$, and during parametric thrust sweeps (up to and including stall) at various combinations of shaft angles and forward speeds. Data were also acquired at conditions matching previous full-scale flight test, small-scale wind tunnel tests and while performing unique slowed-rotor simulations at reduced RPM (40% and 65%), up to an advance ratio of $\mu = 1.0$. Detailed descriptions of these test conditions are presented in Reference 1. A summary of the wind tunnel test conditions can be found in the Appendix.

BLADE DISPLACEMENT SYSTEM

The blade displacement (BD) experimental technique is based on the principles of digital close-range photogrammetry (Ref. 8). Photogrammetry is an optical method that is used extensively to measure aeroelastic deformations of wind-tunnel models (Ref. 9). In this application for the Airloads test, multiple cameras were used to determine the spatial coordinates of retro-reflective targets attached to the lower surface of the blade. These coordinates were then used to extract pitch, flap, and lag, along with elastic bending and twist for each blade of the rotor system. An overview of the test hardware preparation, camera selection, hardware installation and image processing are presented below.

Hardware Preparation

Retro-reflective targets were cut from 4-mil thick, 3M Scotchlite 7610, high reflectance adhesive tape and applied to both the lower surface of the blades and the test section ceiling (Fig. 2). Forty-eight 2-inch diameter retro-reflective

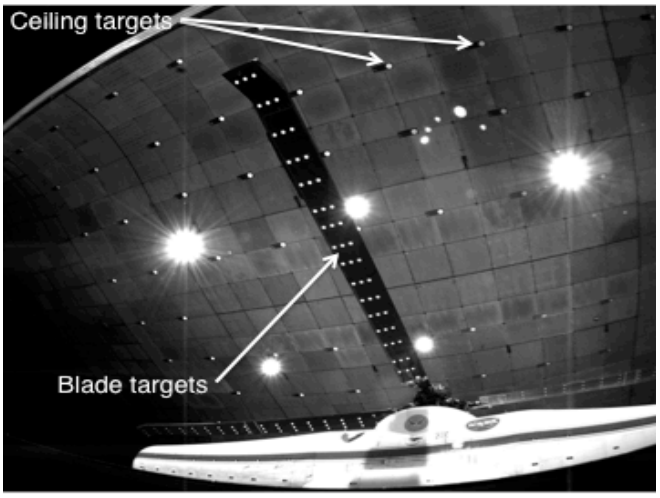

a. Rotor blade and test section ceiling retro-reflective targets.

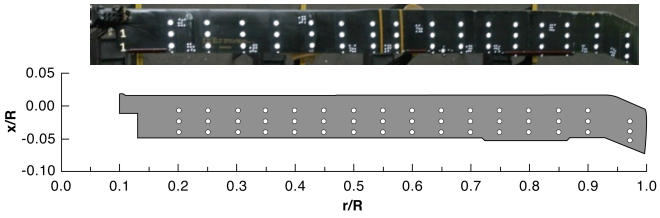

b. Distribution of the rotor blade retro-reflective target radial locations from r/R = 0.20 to 0.97.

Figure 2. Rotor blade and test section ceiling retro-reflective targets.

targets, three per radial station, uniformly spaced at approximately 0.05R intervals between the blade cuff and blade tip, were applied to each blade, covering the blade span from approximately r/R = 0.20 to 0.97 (Fig. 2b). Small blade-to-blade variations in target locations were needed to avoid other surface-mounted blade instrumentation. Eighty-four, six-inch diameter targets were also installed on the test-section ceiling. Next to each ceiling target was a small cluster of 0.5-inch diameter coded targets to assist with automated target recognition, in addition to a single 0.5-inch diameter control target. Blade and ceiling target spatial locations were measured using the V-STARS commercial photogrammetry system, developed by Geodetic Systems Inc (Ref. 10). The standard deviations of the mappings for the ceiling and the blade target measurements were typically less than 0.04 inch and 0.001 inch, respectfully. Further details of the V-STARS measurements can be found in Ref. 11. The mappings of each blade in an un-deformed state and positioned at 0° azimuth serve as reference geometries. The measured spatial data for the blades at any azimuth are then transformed to align with the reference geometry to

determine pitch, flap, lag, elastic twist, and elastic bending. For each blade, the 12 targets at the four inboard radial stations, r/R = 0.20 to 0.35, are used to determine the rigid body motions used to transform all targets. All available blade targets are then used in the computation of elastic bending and twist.

Cameras

The BD system used eight 4-Mega-pixel, 12-bit CCD progressive scan Imperx IPX-4M15-L digital cameras, with a resolution of 2048 × 2048 pixels. The image field-of-view for each camera included a blade azimuth range of at least 90° in order to capture the full motion of each rotor blade with at least two cameras. The overall translational movement experienced by the rotor blades due to angle-of-attack changes, blade flapping and elastic blade deformations further expanded the lens field-of-view requirements. In order to encompass this full range of blade motion and given the camera installation constraints of the test section, Nikon 10.5 mm f/2.8 DX (fish-eye) lenses were selected as a compromise. Short focal length "fish-eye" lenses are not typically used in photogrammetry applications because of the difficulty in obtaining sufficiently accurate distortion corrections. Lens calibrations, mentioned in Reference 11, can partially correct the troubling lens distortions that otherwise reduce the accuracy of the measurements.

Installation

Prior to the start of the UH-60A full-scale wind tunnel test, the BD system setup focused on ensuring high image quality (particularly lighting), optimal orientation angles of the cameras, and adequate coverage on the camera image planes across the complete rotor disk for the anticipated test conditions. A top-view schematic of the LRTA, rotor blades, camera locations and quadrant identifications is illustrated in Fig. 3. The blades rotate counter-clockwise when viewed from above and are numbered 1 to 4. The 0° azimuth location of each blade is aft, over the tail of the LRTA. The four quadrants that make up the rotor disk are defined as Q-I thru Q-IV. Since the rotary shaft encoder 1/rev signal is referenced to blade 1, the azimuth angles of the other three blades must be calculated from the azimuth position of blade 1. The eight BD cameras were positioned such that two cameras predominantly viewed each rotor quadrant. Cameras 1 and 2 view Q-I, cameras 3 and 4 view Q-II, etc. The camera locations were not symmetrical about the rotor shaft due to differences in blade performance on the advancing and retreating side of the rotor, based on experience from the SMART and IBC tests. Figure 4 illustrates the camera port locations in the test section. Although each camera pair was arranged to view a single rotor quadrant, the view from a given camera was not limited to that specified quadrant. In particular, a blade could often be viewed by more than two cameras, resulting in multi-camera photogrammetric intersection of the blade targets at that azimuth.

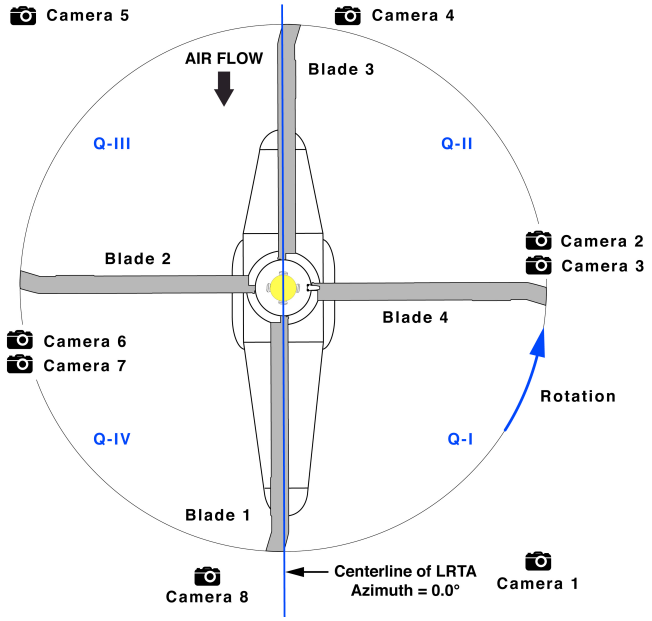

Figure 3. Top-view of the test installation with blade numbers, cameras and rotor quadrants identified.

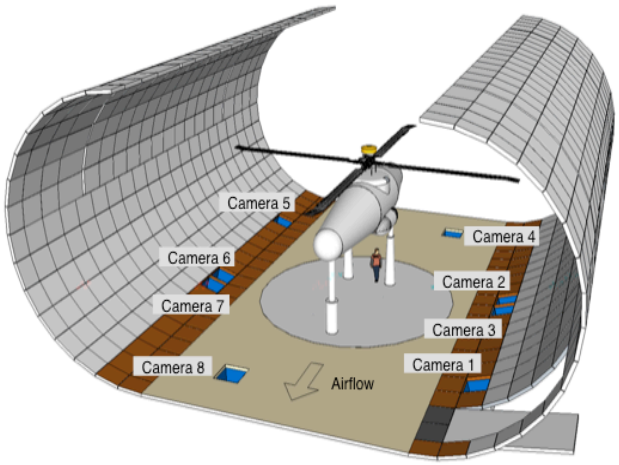

Figure 4. Test section schematic illustrating camera port locations.

The cameras were securely anchored inside the test section floor camera ports, facing upward to view the lower surfaces of the blades through protective low-reflectance glass windows (Fig. 5). These low-reflectance windows were procured especially for the UH-60A test to reduce troublesome reflections from the fiber optic bundle illuminators that can interfere with target centroiding. Target illumination was provided by Perkin-Elmer Machine Vision 7060-10 xenon flash-lamp 50 mJ strobes with pulse duration of 10 microseconds (full width at 1/3 maximum). Fiber optic bundles positioned as near as possible to the optical axis of each camera lens routed the light from each strobe to illuminate the targets. This near on-axis lighting maximized the light return from the blade and ceiling retro-reflective targets. On average, there were (8) 0.25-inch diameter fiber optic bundles encompassing each camera lens to help

distribute the emitted strobe light equally across the blades. Roughly 50% of the fiber bundles were capped with focusing lenses to help increase strobe illumination in areas of the rotor disk (with highly oblique view angle) where the light return from the retro-reflective targets was lower.

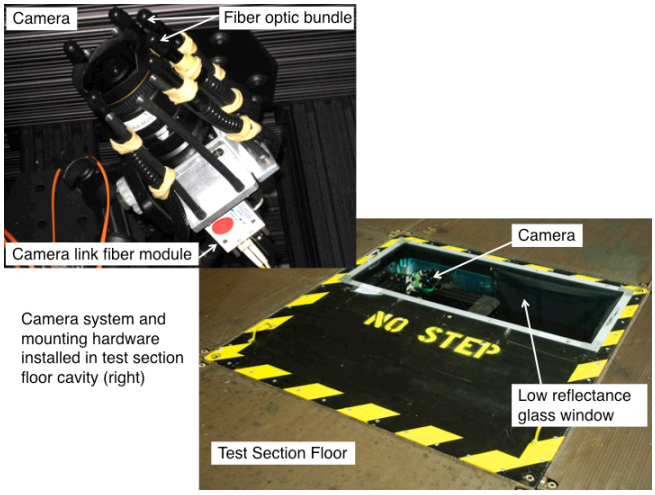

Figure 5. Camera installation inside test section floor cavity.

Data Acquisition

The BD image acquisition hardware consisted of components in both the wind tunnel computer room and in the test section camera ports. The data acquisition system consisted of four PC's running Windows XP Professional®, each with a Matrox Helios PCIX® frame grabber board that was interfaced via Camera Link® through fiber optic cables. Due to the extreme distances (> 250 ft) between the cameras and the BD data acquisition system, Camera Link fiber optic extender units were required to connect data via fiber from the cameras to the PC frame grabber boards. Acquisition software included NASA developed Rotor Azimuth Synchronization Program (RASP) rotor encoder (Ref. 12) and WingViewer image acquisition software (Ref. 13). A digital/delay pulse generator provided the synchronized trigger to the strobes and cameras based on the image acquisition software and RASP selection of azimuth. Four data acquisition systems, one per camera pair, were configured and synchronized. A single BD data acquisition system configuration is illustrated in Fig. 6.

The strobes and cameras were triggered with the strobe light pulses occurring within the integration time of the CCD video cameras and with respect to the desired blade azimuth location which could be set in increments of 0.35° (degree/effective shaft encoder count). All cameras and strobes were synchronized with the rotor shaft encoder to simultaneously capture the retro-reflective targets on the lower surface of each blade at an image-set acquisition rate of once per rotor revolution. Figure 7 illustrates a typical test section camera port installation and LRTA encoder channels.

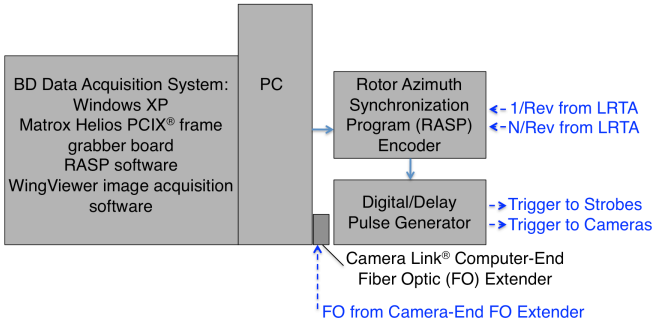

Figure 6. BD data acquisition system computer room components for a camera pair (single rotor quadrant).

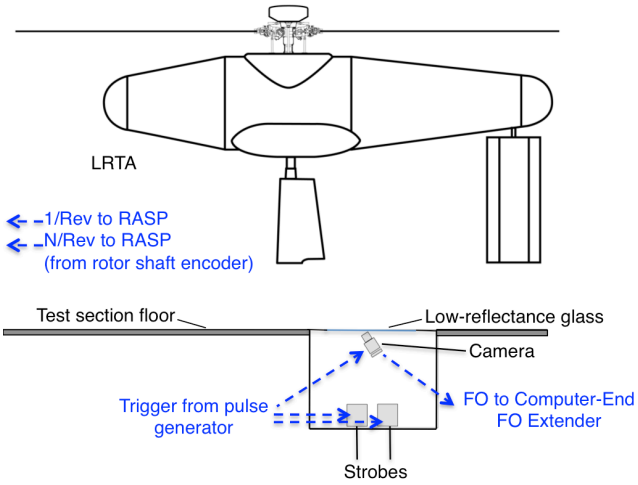

Figure 7. Test section installation of BD data acquisition components in camera port and LRTA encoder signals.

Image data were taken for up to 60 consecutive revolutions to document the instantaneous and mean (via sample average) deformation of each blade at a specified rotor azimuth. This process was repeated for up to 40 rotor azimuth locations to document each blade deformation throughout the entire rotor disk. For the nominal rotor rotation rate of 258 RPM, one image per each of the eight cameras was captured every 0.23 seconds.

BD image data sets were categorized as either primary or secondary. Each of the 27 Airloads primary BD test conditions consist of 60 revolutions of data per azimuth with eight cameras and 40 rotor azimuths, producing 19,200 individual images. The time required to acquire 60 images at each of the 40 rotor azimuths was approximately 14 seconds, leading to a total data acquisition time approaching 10 minutes. The data acquisition time proportionally increased during slowed rotor testing performed at 167 and 105 RPM. Secondary data sets consisted of 12 images per rotor azimuth that recorded a single blade per rotor quadrant for a data set of 11 azimuth positions over a range of 95°. Acquisition time for secondary data sets was approximately one minute. These secondary data sets were acquired during the majority of the Airloads wind tunnel test, during test conditions not identified as BD primary data points. The highlighted test

conditions in the Appendix are considered the primary BD conditions.

DATA ANALYSIS

Image Processing

Each test condition consists of a 12- or 60-image set at each azimuth station. Each set of images was digitally processed to calculate centroid locations of discrete targets on the rotor blades and test section ceiling. For image processing and data reduction, a suite of custom designed image processing and data reduction functions were developed using the Mathworks® Matlab software environment. Supporting functions for image processing, photogrammetry, and coordinate transformations are provided via a custom Matlab Photogrammetry Toolbox developed for NASA by Western Michigan University (Ref. 14). This toolbox, in conjunction with the Matlab Image Processing and Statistics Toolboxes, were integrated into a NASA rotor-specific toolbox suite of functions. The NASA Rotor Toolbox makes use of moderately automated post-test image processing procedures that identify and calculate the image plane centroid spatial coordinates for each target. The Rotor Toolbox also contains a number of specialty scripts and functions for camera calibration, determining camera location and pointing angles, performing multi-camera intersections to determine 3D spatial coordinates computing pitch, flap, and lag angles as well as elastic bending and twist.

An interactive graphical user interface (GUI) is used for image processing of targets and target centroid inspections. The display on the GUI panel shows the Project, Centroid, and Image paths to assist the user with information about the current data point. Interactive options are available for selecting a camera, blade, run number, point number, and image grayscale threshold.

The GUI contains several centroid processing and inspection features. For example, with the GUI a specified image set can be processed to compute grayscale centroids. Another GUI option allows centroids to be superimposed onto images for data inspection. A convenient option, particularly when images are not available, plots the centroid locations for every revolution without superimposing them onto an image. This option is useful for viewing the rev-to-rev spread of targets on a single plot.

Target and centroid inspections can be tedious because of subtle complications to the centroiding process. A GUI option can be used to create a centroid summary file in which missing centroid files can be detected. Partially blocked targets, for instance, can be difficult to detect because they are sometimes identified as full size targets. These occurrences are problematic because the target centroids are offset and not properly defined. In addition, targets with very weak or saturated grayscale can sometimes reduce centroiding accuracy. Another GUI option is available to conveniently correct or remove mislabeled or suspect targets once identified without having to reprocess the entire image set.

Due to the movement of the rotor blades about the image plane and target numbering confusion caused by blocked targets, a user interface is necessary for the first image of each data sequence. Figure 8 shows a sample of the blade centroids being identified by this initial processing step. After target numbering is properly identified using the first image, the computation of target centroids for the second image thru the end of the image sequence is fully automated. Targets on the LRTA fuselage, test section ceiling, and instrumentation hat are useful visual guides during this processing step.

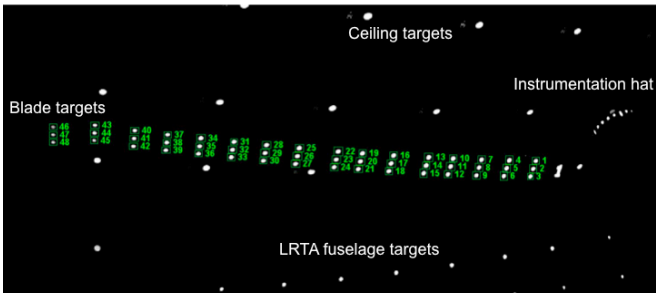

Figure 8. Image processing example with the identification of rotor blade targets.

A separate centroid validation Matlab function was also developed to locate mislabeled or suspect centroid data that may require manual correction. For example, slowed-rotor, high advance ratio test conditions proved to be particularly challenging due to the extreme image-to-image blade motion (compared to lower advance ratios). This holds true even near the inboard portion of the rotor blades. Also, ceiling targets and strobe window reflections have the potential to interfere with the accurate identification of blade target centroid locations. These two image processing challenges are described in the following section.

Centroid Validation

Centroid data must be inspected and validated since an image set may contain targets that appear in several images of an image sequence, but disappear (either fully or partially) in later images of the same sequence (Fig. 9). Figure 9a is a long-exposure close-up of the LRTA and inboard portion of the rotor blades with the blade area of interest indicated within the red box. Figures 9b and 9c are two data images from the same image sequence where the trailing edge targets of blade 1 can be seen in Fig. 9b, but are no longer visible in the next image, Fig. 9c. As the blade flaps the trailing edge targets are intermittently blocked by the LRTA fuselage. This increases the difficulty in automating the image processing.

Strobe reflections have also proven to be challenging for implementing automation of the image processing. The light from the xenon strobe reflecting off the camera port window can be seen in each image of Fig. 10. Although the reflection

a. Close-up of LRTA with region of interest for Figs. 9b and 9c.

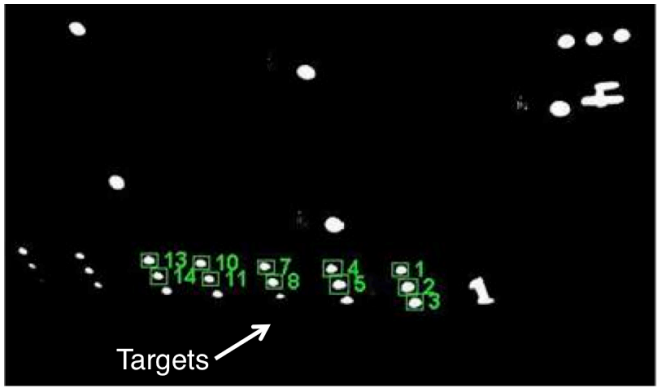

b. Trailing edge targets of Blade 1 are visible.

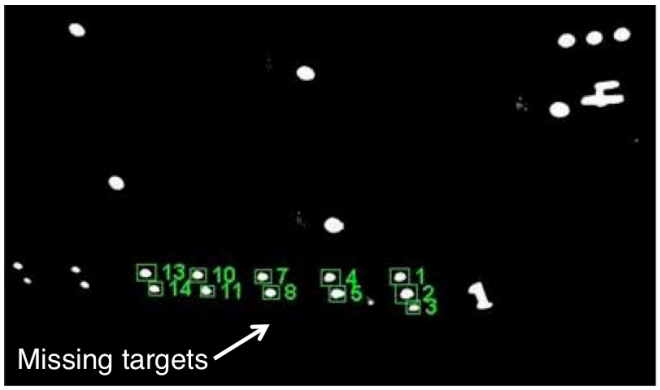

c. Trailing edge targets of Blade 1 become blocked by the LRTA fuselage.

Figure 9. Example of blade targets blocked by the LRTA fuselage for images from the same data sequence.

intensity has been reduced by a factor of approximately four by replacing the standard glass camera port windows with low-reflectance coated windows, they continue to pose potential complications with image processing automation. The reflections generally affect only a few targets on each blade at a single blade azimuth position per camera (Fig. 10a). Consequently, rev-to-rev variations in blade position can cause the strobe reflections to intermittently merge with blade targets. Figure 10b illustrates two blade targets near the vicinity of a strobe reflection where the blade target is properly discriminated. However, in the same image sequence, the strobe reflection can merge with an adjacent

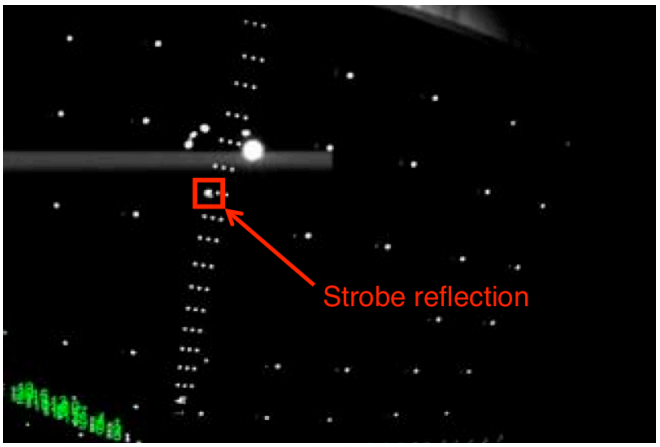

a. Typical image with strobe reflection near the vicinity of blade targets; Red box indicates area of interest for Figs. 10b and 10c.

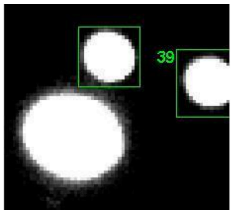

b. Image showing strobe reflection distinct from targets.

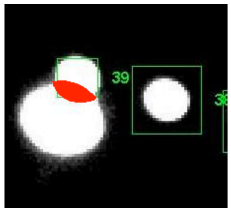

c. Image showing strobe reflection overlapping blade target; red region indicating combined grayscale.

Figure 10. Effect of strobe light reflection combining with target centroid.

target as indicated by the shaded red area of Fig. 10c, causing an error in the centroid location. More effective means for dealing with these occurrences and improving the level of automation are needed.

MEASUREMENT PROCESS UNCERTAINTY CONSIDERATIONS

Estimates of Static Precision and Limited Bias

The uncertainty of blade displacement measurements consists of both precision and bias errors. Precision errors of the measurement process define the variation (or scatter) in repeat measurements due to random processes. It is a measure of the capability of the experimental technique to discriminate between two measurements. The precision error of the measurement process can be estimated from the standard deviation of repeat measurements when everything is held constant. It is important to separate the precision of the BD measurement technique from the experimental variations that occur when the blade oscillates (especially evident when the blade is rotating and under flow conditions). For instance, large values of the standard deviation noted during blade rotation and with flow are due to blade motion, not scatter from the measurement technique. The other component of the uncertainty, bias (or systematic) error, are those errors that do not contribute to the scatter. The bias error can be thought of as a mean offset

from the true value with a scatter about that mean given by the precision. Bias errors for optical measurement techniques applied to wind tunnels are particularly difficult to accurately quantify. However, a limited first estimate of the precision and bias errors for the BD measurements in a static measurement situation can be very useful to identify and possibly improve the uncertainty of the measurements without the complications of rotating blades and airflow. The limited and incomplete results presented here, while not a formal uncertainty analysis, can help explain the strengths and weaknesses of the BD measurement system. A more extensive uncertainty analysis is needed to include the effects of a rotor operating in forward flight.

In order to provide an estimate of the static precision and bias of the measurement technique without the complications of rotating blades and airflow, a static wind-off azimuth sweep over 360° was taken. (Note that this static sweep is also used for testing ongoing improvements to the data reduction procedures.) Forty blade azimuth angles were set by manually positioning blade 4 over a range of 360°. The LRTA shaft encoder determined the azimuth for blade 1 at each azimuth position. The azimuths of the other three blades were then calculated based on the azimuth of blade 1. The initial estimate of static precision is taken to be the standard deviation of repeat measurements at a single azimuth. A total of 160 data points (40 for each blade) at three images per data point were taken. The mean of the standard deviations of the 160 points for each parameter is used to approximate the standard deviation of repeat measurements at a single azimuth to yield a rough estimate of static precision.

Each blade should have nearly identical values of pitch, flap, lag, elastic bending and twist independent of azimuth. Thus deviations from the mean value over 360° azimuth indicate error in the BD measurement, which contributes to the total bias error. This component of the bias error is a function of azimuth and, if found to be repeatable, could be removed from subsequent measurements. The limited bias error representing variations with azimuth was computed as the standard deviation of the 160 sample means over 360°. The results for initial estimates of precision and the azimuthal component of bias error from a static sweep for pitch, flap, and lag in terms of one standard deviation are presented in Table 2. Other important factors leading to additional error in the measurement process not reflected in the following two tables are discussed later in this section.

Table 2. Estimates of static precision and bias based on static, wind-off measurements over 360°.

	Precision	Bias
Pitch	0.007°	0.267°
Flap	0.007°	0.372°
Lag	0.002°	0.366°

Similarly computed results for elastic bending in Z and elastic twist, along with the inboard and outboard Z-coordinate of a single target are presented in Table 3. Note the good precision at a single azimuth for Table 2 and for the inboard data of Table 3. This data emphasizes the ability to discriminate rev-to-rev differences over time for a blade at a given azimuth and condition, even in the presence of significant bias error.

Table 3. Estimates of static precision and bias based on static, wind-off measurements over 360° at inboard (r/R = 0.20) and outboard (r/R = 0.97) stations on the blades.

	r/R	Precision	Bias
Elastic Z	0.20	0.002 in	0.098 in
Elastic Twist	0.20	0.012°	0.200°
Z	0.20	0.002 in	0.432 in
Elastic Z	0.97	0.038 in	1.122 in
Elastic Twist	0.97	0.025°	0.229°
Z	0.97	0.066 in	1.429 in

In addition, blade-to-blade differences at a given azimuth can be effectively discriminated. It is important here to separate the precision of the measurement technique from the experimental variations that occur when the blade oscillates in the vertical direction. This is especially evident when the blade is rotating and under flow conditions. An example of blade motion can be seen even in the static data of Table 3 by comparing the precision at the inboard and outboard radial blade positions r/R = 0.20 and 0.97. For the inboard radial position r/R = 0.20 the movement of the blade during image acquisition is nearly negligible and more indicative of the precision of the measurement technique. However, at the outboard radial position r/R = 0.97 significant and measurable vertical blade motions occur as the blade is moved to a new azimuth, mainly due to the sizeable length (322 inches) of the rather narrow blades (≈21 inch chord). For the static sweep, blade 4 was manually positioned to the desired azimuth at a rate of about one point per minute. The manual pushing of blade 4 to each new azimuth caused a 2× change in lag variation compared to the other three blades. The one point per minute manual positioning of the blades did not allow enough time to settle before taking image data and moving on to the next azimuth position. Thus the data at r/R = 0.97 includes both experimental technique precision (of the order shown by the inboard data at r/R = 0.20) as well as the variation in the blade motion. For example, the Z-coordinate near the tip, on average, has a value 33 times greater than the inboard portion of the blade in Table 3. Therefore the inboard data is a better indicator of the experimental technique static precision for elastic Z and elastic twist. Note that generally pitch, flap, and lag are determined from the inboard portion of the blade from r/R = 0.20 to 0.35, so that their values of precision presented in Table 2 are impacted much less by blade tip motion.

As is often the case for optical techniques applied to wind tunnel measurements, the bias errors are larger (and generally more difficult to quantify) than the precision. Over

a range of 360°, the static bias errors for the parameters pitch, flap, lag, elastic Z, and elastic twist can be significant. Part of the bias error is caused by the use of a different set of cameras to measure a given blade as it rotates about the shaft. Possible ongoing enhancements to the data reduction procedures such as optimization of camera calibration coefficients (briefly discussed later in this section), alternate fish-eye corrections based on equisolid angle projection, and weighting of multiple intersection *XYZ* results by the variance can be tested utilizing the available static data set to assess any improvements (or detriments) in the bias error.

Mean Bias offset for Pitch, Lag, and Elastic Twist

The values of flap angle, lag angle, and elastic Z are not necessarily known for the static sweep, thus their mean values over 360° cannot be easily compared to known reference values to determine a measure of bias offset error. However, the root collective pitch angle was set to 0° and the elastic twist is expected to be near zero throughout the static azimuthal sweep. Thus for these two parameters the mean difference from zero over the 360° azimuthal sweep can be viewed as a bias offset error. The mean bias offset error over 360° for pitch and elastic twist are presented in Table 4 at the radial station $r/R = 0.97$. Note that the error in the root collective is thought to be around 0.2°.

Table 4. Mean bias offset error based on static, wind-off measurements over 360° for *r/R* = 0.97.

	Bias
Pitch	0.102°
Elastic Twist	-0.023°

Error Due to Rigid Body Transformation

A source of bias error not reflected in the tables and discussion above is the use of inboard targets from $r/R = 0.20$ to 0.35 for the 3D nonlinear least squares coordinate transformation of the blades to each of the four reference geometries at 0° azimuth. This transformation is necessary in order to separate and resolve the much smaller elastic deformations from the rigid body motion that occurs as the blade rotates about the shaft, coupled with additional changes in pitch angle and flap that are azimuth dependent. It is important to emphasize that the blade displacement values of pitch, flap, and lag, while useful for comparisons, are primarily used to remove rigid body motion in order to compute the elastic deformation of bending (Z) and twist. It is the elastic deformations that are the most important product of the blade displacement measurements.

The determination of the rigid body motion of the blade targets begins with a 3D conformal transformation about the cross-flow coordinate of the wind tunnel based on the facility value of the shaft geometrical angle of attack α_s. This is a forward transformation and no additional parameters are determined from this operation. The α_s transformation is used to align the z-axis of the blade target data parallel with the rotor shaft. Any error in the facility value of α_s causes error predominantly in pitch (which varies as the sine of azimuth) and flap angle (which varies as the cosine of azimuth). A jitter test with ± 1° error in α_s for the $\mu = 0.30$ flow case discussed later confirms the sine and cosine dependences for pitch and lag to within 0.04° worse case. This same jitter test produces a worse case error for lag of 0.08°. The error is less than 0.01° for elastic bending or twist for ± 1° error in α_s. The reason no error is noted for elastic bending or twist is that the computed transformation coefficients (discussed next) completely compensate for any error in α_s.

A non-linear least squares 3D conformal transformation solver is next used to align the measured blade coordinates with the reference geometry (which varies slightly blade-to-blade due to small targeting differences between the blades). The most inboard 25% of the available targets are used for this transformation solver. The solver yields three Euler angles and three translation terms based on these inboard targets. The three Euler angles are taken in the standard XYZ order, with omega about X, phi about Y, and kappa about Z. These Euler angles are related to pitch, flap, and lag, but have a common hinge centered on the rotor shaft. Thus while these three angles only approximate pitch, flap and lag, they do provide a means to remove most, but not all, of the rigid body motion that can be much larger than the elastic deformations. Modifications to the data reduction to include ZYX order of rotation and location of the center of rotation for flap and lag at the effective blade hinge should be considered. The three Euler angles and translation terms are then applied in a forward 3D conformal coordinate transformation to all the blade target coordinates (after the above rotation by α_s). The pitch axis, after transformation, is at the nominal quarter-chord distance from the leading edge, while neglecting small changes in the quarter-chord that occur along the blade due to sectional changes in airfoil shape. Thus the final inboard target coordinates are aligned with the reference geometry, but elastic bending and twist will cause slight deviations of the outboard portion of the blade from the reference geometry. To compute elastic bending and twist, the chordwise slope angle and z-intercept at each radial location r/R (three targets per row) are then computed for the reference geometry and for the transformed measured targets. The elastic bending is taken to be the difference of the measured z-intercepts from the z-intercepts of the reference geometry. Elastic twist is taken to be the differences in slope angles between the transformed measured target coordinates and the reference geometry at each r/R radial station. The induced twist of the lower surface targets measured in this manner is assumed to follow the induced elastic twist of the displaced blade chord line.

The bias errors for pitch and lag, while not negligible, do not indicate a major concern for the computation of elastic deformation at this time. However, that is not the case for flap, which has a much larger potential bias error. While little flap angle bias error is noted for near-zero bending, significant bias error in flap is noted for non-zero elastic

bending. The error in flap is a direct consequence of the slope in the *Z*-coordinates as a function of *r/R* due to residual elastic bending from *r/R* = 0.20 to 0.35. The bias error in flap leads to slope error in the 3D coordinate transformation to the reference geometry. The slope error in the 3D coordinate transformation causes a slope error in elastic bending and twist that causes those results to be underestimated. A search is underway for robust methods to compensate for this effect. In addition, investigations are underway with an alternate method that does not depend on the inboard targets for transformation.

Bias Error Correlation for Elastic Deformation

The bias error for the elastic deformations can be lessened significantly for closely spaced targets when their bias error in Z is correlated. For example, the bias error for elastic twist has extreme sensitivity to errors in the *Z*-coordinate of a single leading edge or trailing edge target at a given normalized radial position, *r/R*. The limited separation of leading and trailing edge targets, *L*, places a lower limit on the error in the determination of elastic twist. As a simple limited example, if the total error in *Z* between the leading and trailing edge targets δZ is 0.01 inch, the error in elastic twist angle $\delta twist$ (neglecting any error in the separation of the targets) is 0.05° based on a simplified error expression using the arcsin of the ratio of δZ *to* *L* with *L* ≈10.5 inches. Note however, the more important error in the *difference* between leading and trailing edge targets can actually be much smaller than the absolute error in the *Z*-coordinate of either target due to correlation in the error. Thus elastic twist and out-of-plane bending (Z) can be determined to an uncertainty significantly less than that indicated by considering the bias errors in Z separately (and uncorrelated). In fact, the uncertainty can even approach the much smaller values of precision for very closely spaced targets. The degree of error correlation depends primarily on the separation of the targets on the image plane. Closely spaced targets on the image plane will have similar correlated errors, even when the following error sources are present: (1) incomplete distortion correction, (2) fundamental limitations due to camera view geometry, (3) errors in camera parameters such as camera constant, photogrammetric principal point, horizontal and vertical pixel spacing, (4) image sensor non-uniformities, (5) error in camera location and pointing angles, and (6) errors in the mathematical model used for distortion correction. As the separation between targets increases, such as from near the tip to inboard, the correlation decreases markedly. Little error correlation occurs for large changes in azimuth.

Optimization of Camera Calibrations

The optimization of camera calibration coefficients is currently under investigation. Optimization may improve the camera calibration coefficients for improved 3D coordinates along with improvements in the computation of pitch, flap, lag, and elastic bending and twist. In addition, optimization may automate and significantly reduce the amount of time necessary to identify and eliminate outliers of the processed data. Techniques for fine-tuning the camera calibrations used a static data set acquired over the full rotor azimuth, 0° shaft angle and three images per azimuth.

The test section ceiling targets enable the determination of the external camera calibration coefficients, specifically the three camera position coordinates and three angles for the eight cameras. Given these camera calibration coefficients and multiple views of a blade, many intersection combinations are possible to determine specific target *XYZ* coordinates. An example of multiple intersections to determine alternate sets of target coordinates is shown in Fig. 11 plotted in the wind tunnel coordinate system. (The corresponding Figs. 12 and 13 are also in the wind tunnel coordinate system.) The *XY* coordinates of the blade targets translated to the chord line and the coordinates of the quarter-chord for all possible camera combination intersections of blade 1, are shown in Fig. 11a. The data includes the entire static azimuth sweep for each of the 16 blade radial stations. These 40 azimuth positions represent

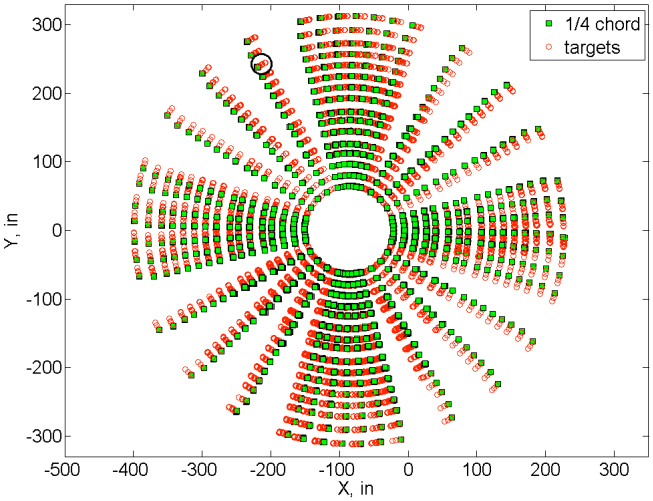

a. 1/4 –Chord XY coordinates and target XY coordinates transferred to the chordline for blade 1.

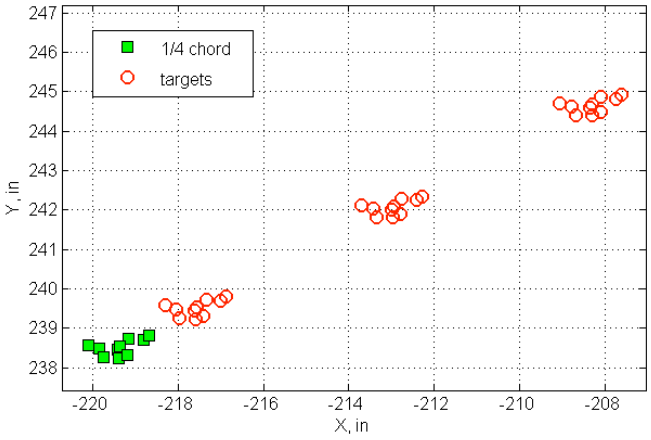

b. Zoomed in view of the XY coordinates of blade 1 at ψ = 120° and r/R = 0.85.

Figure 11. XY target coordinates for non-optimized exterior camera calibrations.

the same angles used in the primary data acquisition sequences. The series contains 15° increments throughout the entire azimuth sweep and 5° increments about the 0°, 90°, 180° and 270° regions. A set of targets located at ψ = 120° and r/R = 0.85, is circled in Fig. 11a and is enlarged in Fig. 11b. The data are from 10 different combinations of intersections available at this location and the coordinate results have a scatter approaching ± 1 inch.

Of the several approaches considered to optimize the exterior camera calibrations, preliminary results for the best approach to date are illustrated in Fig. 12. For this approach the composite standard deviation of the camera intersection standard deviations, averaged over all points, all blade azimuth angles, and all intersections for the entire static data set were optimized. The resultant optimized camera calibration values, while time-consuming to determine, reduce the scatter by roughly a factor of three. Figure 12 shows the same enlarged blade station noted in the baseline case, Fig. 11a, showing the targets with a tighter grouping after optimization.

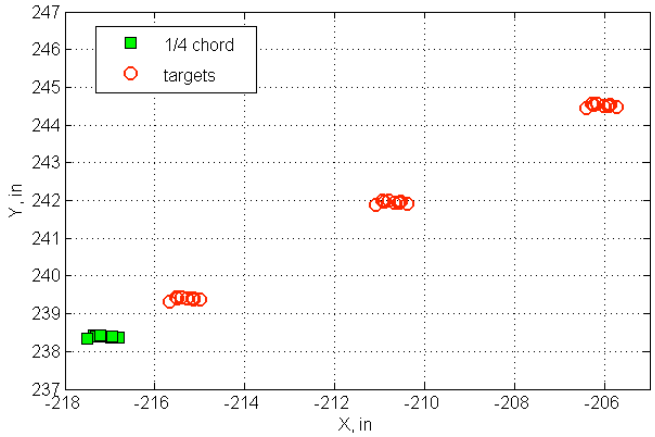

Figure 12. XY target coordinates for optimized exterior camera calibrations. Zoomed in view of the XY coordinates of blade 1 at ψ = 120° and r/R = 0.85.

Another assessment of the calibration coefficient optimization technique is shown in Fig. 13. Blade 1 contour plots of the measured airfoil section quarter-chord Z-displacement for the static case are shown in Fig. 13. For static data taken at 0° shaft angle, Z-displacement contour plots are expected to be nearly concentric circles. A comparison between results using the non-optimized camera calibration coefficients and results using the optimized calibration coefficients are shown in Figs. 13a and 13b, respectively. The optimized camera calibration coefficients results are noticeably more symmetric than the non-optimized results. Developments of the camera calibration optimization technique are expected to continue to assess the degree of improvement over non-optimized results.

Comparison Between Experiment and Computation

The comparison between experimental and computational blade displacements is important for the validation of both. Agreement tends to initially validate both, whereas disagreement leads to further investigation to ascertain possible sources of error in either set that might help explain the disagreement. Reference 15, while discussing first comparisons of experimental data and computational results from this same test, summarizes with the following: *Unfortunately, not all test data is perfect and no simulation is exact. The goal of this work is to provide an initial correlation between measured data and a state of the art simulation. This correlation is intended to help discover flaws in experimental technique while at the same time identifying opportunities to enhance rotorcraft simulation technology*. Thus the determination of likely experimental measurement bias error (even without estimates of the magnitude of such errors) is critical for properly interpreting these comparisons.

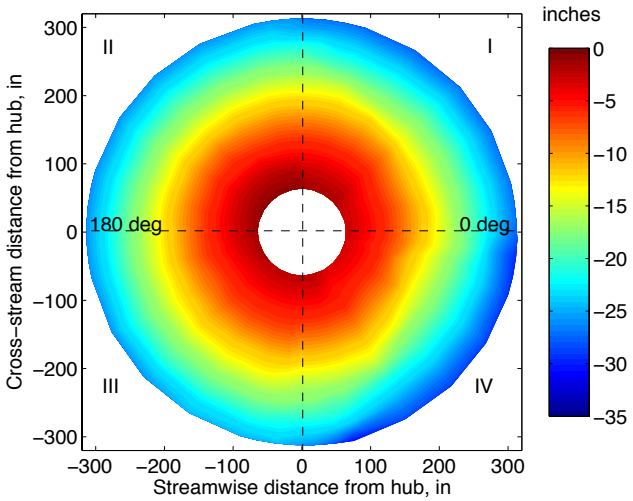

a. Z-displacement with non-optimized camera calibration coefficients.

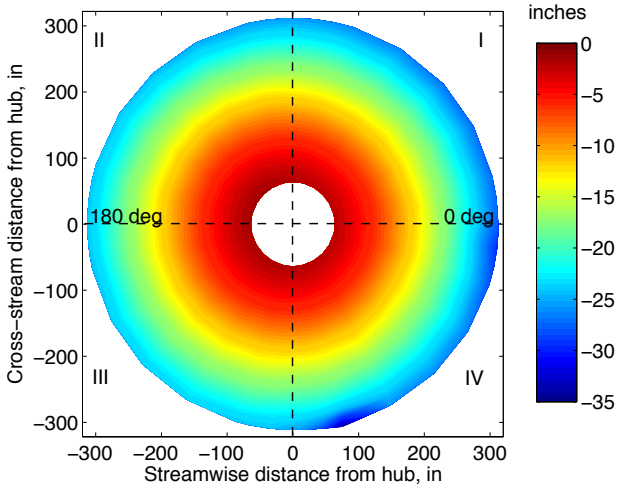

b. Z-displacement with optimized camera calibration coefficients.

Figure 13. Z-displacement of airfoil-section ¼-chord points for Blade 1, static case, α = 0°.

Several complications arise when comparing experimental and computational results. For example, it is typical in computational results to use shaft *Z*, *Y*, *X* order for angle rotations, whereas for experimental results it is more common to use *X*, *Y*, *Z* order. Also, the rotation about the shaft *Z*-axis (used to specify azimuth) is at the center of the shaft, whereas the accompanying lag angle center of rotation (as well as flap angle) is offset by 15 inches and rotates about the shaft axis. Due to the built-in pre-lag of the blade about the elastomeric hinge, coupled with the change in lag angle for various flow conditions, the rotation axis for pitch varies with respect to the blade as test conditions are varied and is not necessarily always about the quarter-chord reference axis of the blades (Ref. 16).

The computed normalized displacement variables are typically expressed in a so called *motion* file (Ref. 17) by *dx*, *dy*, and *dz* which represent the displacement in the *X*, *Y*, *Z* axes, normalized with respect to the blade radius $R = 322$ inches. Also contained within the computational *motion* file are the Euler angular changes in degrees about the *X*, *Y*, and *Z* axes *dxang*, *dyang*, and *dzang*. Each of these variables is a function of both azimuth ψ and normalized blade radial position *r/R*. The reference quarter-chord normalized locations in *X*, *Y*, *Z* are given within the *motion* file by *xqc*, *yqc*, and *zqc*. Since the elastomeric hinge point of the blade is located at $r/R = 0.0466$ (Ref. 16), computational data typically presented at *r/R* intervals of 0.01 will show the first non-zero values at $r/R = 0.05$.

RESULTS AND DISCUSSION

The sample results presented here are for a moderate advance ratio test condition. Preliminary CFD comparisons with the moderate advance ratio case will also be presented.

The CFD comparison data presented here is computed using a loosely coupled technique wherein high-fidelity Navier-Stokes aerodynamics are provided by the OVERFLOW-2 code and structural modeling and trim are provided by the CAMRADII software. This technique was pioneered by Tung et al. (Ref. 18) and later implemented in OVERFLOW by Potsdam et al. (Ref. 19). Significantly improved aerodynamic and structural load prediction capability has been demonstrated for the UH-60A rotor in steady level flight conditions using this approach (Ref. 15).

The measured V-STARS blade targets from $r/R = 0.20$ to 0.35 at the 0° azimuth position represent the un-deformed reference geometry. Comparing these inboard blade targets of the measured blade data and the V-STARS reference geometry using a nonlinear least squares three-dimensional conformal transformation solver provides three Euler angles and three translations. The three Euler angles from the transformation solver define the approximate inboard pitch, flap, and lag (with proper attention given to sign, blade number, and azimuthal restriction of range from 0° to 359.9…°). The BD measured angles can be compared to the traditional mechanical blade motion measurements and the laser-based blade measurements, each of which were used during the Airloads wind tunnel test. (See the section above on Measurement Process Uncertainty Considerations for differences between the BD and facility definitions of pitch, flap, and lag angles.) This comparison can help validate and resolve potential discrepancies between the measurement methods, as well as help define any blade-to-blade differences. Because the BD measurements use the same set of cameras to measure all four blades, they are expected to be more consistent for rev-to-rev and blade-to-blade comparisons. Thus any BD bias errors that are common to all four blades will generally be subtracted and removed when these comparisons are made. The CFD/CSD technique models each blade identically and hence exhibits no blade-to-blade differences. Blade-to-blade differences uncovered by the experimental technique may prove to be useful to provide a range of valid blade geometry inputs to CFD/CSD.

Moderate Advance Ratio Case with CFD Comparison

The following results are for one moderate advance ratio primary BD condition: $\mu = 0.30$, $C_t/\sigma = 0.10$, $\alpha_s = 0°$ and $M_{tip} = 0.65$, representing a single data point from the airloads Parametric Sweep Conditions (Appendix). The sample results highlight preliminary BD measurements for four blades over the full azimuth range: 1) pitch, flap and lag, 2) out-of-plane elastic deformation in the vertical direction and elastic twist, including a sample of rev-to-rev variations of elastic data versus *r/R*, and 3) vertical location of the blade tip and inboard portion of the blade, showing blade-to-blade differences.

Figures 14-16 illustrate pitch, flap, and lag angles with computational data overlays and blade-to-blade differences vs. azimuth angle. Each of the data points in these figures are time averages of 60 consecutive rotor revolutions at each azimuth. Blade-to-blade differences are emphasized by subtracting at each azimuth, the mean value of the four blades at that particular azimuth.

Included in Fig. 14a are preliminary CFD/CSD predictions for blade pitch. The *commanded pitch* is an estimate of the fixed system root collective indicated by the rotor control pushrod positions. The “NFAC meas” data is the pitch as measured at the blade root by the crab arm or laser system. The accuracy of these measurements is under review, but believed to be accurate to within 0.2°. The predicted data match the commanded and measured blade pitch closely in trend but exhibit a mean shift of approximately 2°. This result is common in coupled CFD predictions and results from incomplete force conservation during coupling with CSD along with CFD’s inability to accurately predict the lift-curve slope for this blade. Note that for the computational results, the collective and cyclic are adjusted to meet specified trim targets (Ref. 15). Thus the offset of the experimental and computational results for pitch reflects this adjustment and does not necessarily indicate a problem with the experimental results. Note that the commanded and NFAC measurements are in close agreement with the BD measurements. Figure 14b shows the

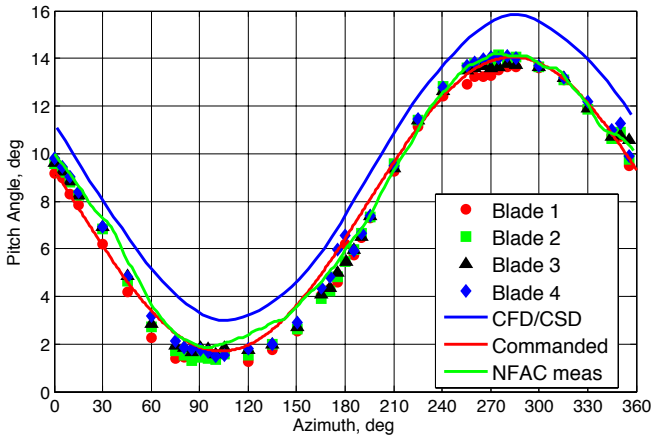

a. Blade 1-4 pitch angle, CFD/CSD predictions, NFAC measured and commanded pitch vs. azimuth.

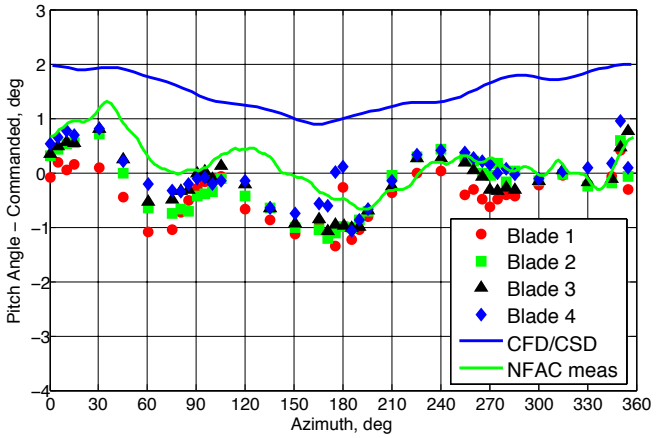

b. Pitch angle – commanded pitch, CFD/CSD, NFAC measured pitch vs. azimuth.

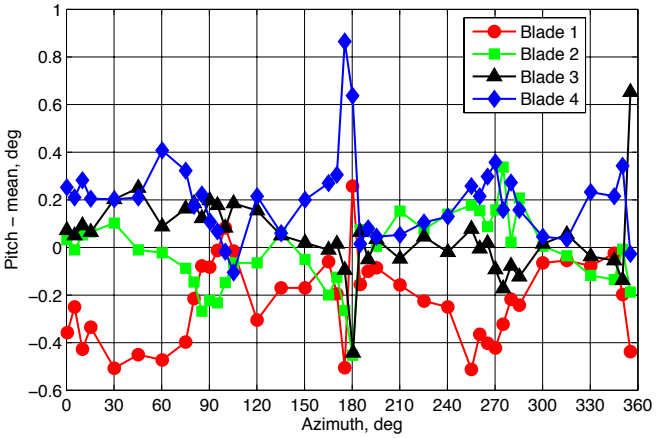

c. Blade-to-blade differences in pitch angle vs. azimuth.

Figure 14. Blade pitch angle vs. azimuth, $\mu = 0.30$, $C_T/\sigma = 0.10$, $M_{tip} = 0.65$.

BD measurements of pitch for all four blades, CFD/CSD, and NFAC measurements of pitch all plotted with the commanded pitch subtracted (note the expanded vertical axis). Figure 14b shows that generally the BD measurements and the NFAC measurements agree with only occasional disagreements up to 1°, whereas BD measurements and CFD/CSD have an offset of about 2°.

The blade-to-blade differences in pitch are plotted in Fig. 14c. Blade 1 has a slightly lower pitch angle over most of the range. The identification, removal, and/or correction of possible outliers such as those associated with Blade 4 at 175° and 180° azimuth, are currently under review.

Flap angle versus azimuth and the corresponding flap angle blade-to-blade differences are shown in Fig. 15. The mean flap angle for all four blades over 360° is 4.89° with a standard deviation of each blade over the entire azimuth that ranges from a low of 0.46° for Blade 2 to a high of 0.61° for Blade 3. The data measured by the crab arm are included as the green line in Fig. 15a. These measurements are intended for general comparison since their accuracy is unverified. The blade-to-blade differences in flap for the moderate advance ratio condition are plotted in Fig. 15b. For the BD measurements, the largest flap angle differences occur between Blade 1, the pressure instrumented blade, and Blade 3, the strain gauge instrumented blade, at an azimuth range

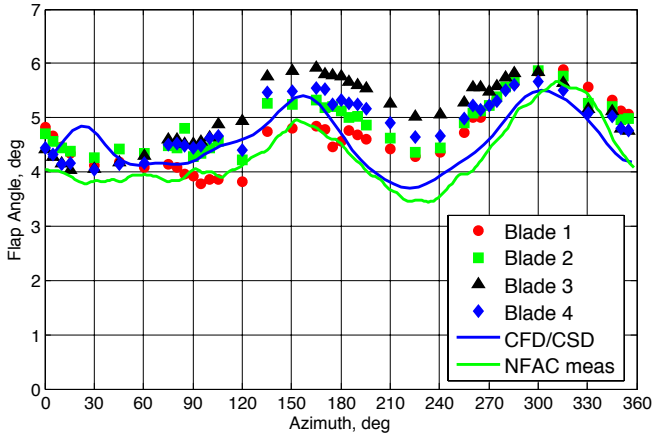

a. Blade 1-4 flap angle and CFD/CSD predictions vs. azimuth.

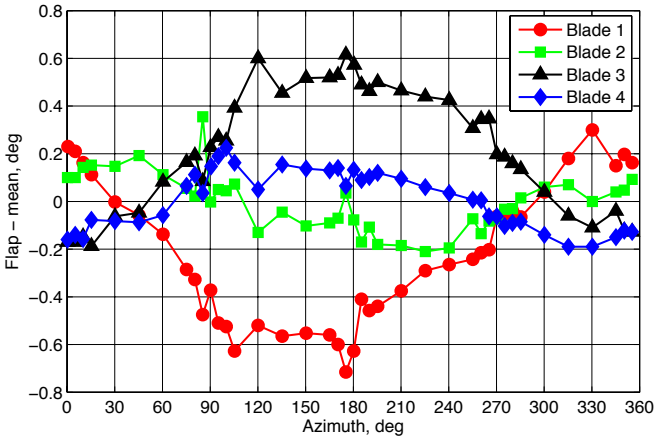

b. Blade-to-blade differences in flap angle vs. azimuth.

Figure 15. Blade flap angle vs. azimuth, $\mu = 0.30$, $C_T/\sigma = 0.10$, $M_{tip} = 0.65$.

of 60° to 270°. The maximum flap angle difference is nearly 1.1°, with the mean values of flap over 360° for blades 1 and 3 differing by 0.44°. Blades 2 and 4 are not instrumented and in better agreement with a mean value over 360° equal within 0.01°, and a maximum measured difference of 0.3°.

The CFD predicted flap angle in Fig. 15a is in good agreement with measured data both in mean and trend. Accurate prediction of flap angle is largely dependent on two factors: accurate knowledge of blade spanwise mass distribution and accurate thrust prediction. Since the CFD model was trimmed to match the measured thrust coefficient, thrust correlation is implicitly exact. The degree to which the measured and predicted flap angles agree in Fig. 15a is therefore an indication that the blade spanwise mass distribution is reasonably well modeled.

Lag angle versus azimuth and the corresponding blade-to-blade differences are presented in Fig. 16. Positive lag indicates that the blade is lagging relative to the shaft azimuth reference angle. The lag data shows blades 1, 2, and 4 with similar lag profiles to within ≈ 0.1°, whereas Blade 3 on average leads the other three blades by 0.32° independent of azimuth. The standard deviation of the blade-to-blade differences for each blade over the full azimuth are less than 0.06°, which indicates very little blade-to-blade azimuth variation in lag in addition to providing an estimate of the potential precision in measuring lag for the rotor system at this flight condition.

CFD-predicted lag angle correlates well in trend but poorly in mean with the BD measurements and NFAC measurements of lag. Successful prediction of lag angle is dependent on accurate prediction of torque coefficient and accurate knowledge of blade chordwise mass distribution. Like the spanwise mass distribution, the chordwise mass distribution is believed to be reasonably well known. In this case the discrepancy in mean values is partially due to an over predicted torque coefficient (measured $C_Q/\sigma = 0.0038$ vs. predicted $C_Q/\sigma = 0.0047$). If the predicted torque were lower the mean lag would decrease, however it is unlikely that this would account for the entire difference observed in Fig. 16a. Further study is required to fully understand this difference in mean lag.

The three-dimensional transformation coefficients of the rigid body motion at the root were determined from the inboard 25% of viable targets. The measured XYZ coordinates (corrected for shaft angle) from the wind tunnel coordinate system were transformed to the rotor coordinate system aligned with the reference geometry. Linear fits are made to determine slope and intercept in the YZ plane of the reference geometry and also the transformed measured blade at each of 16 radial stations. Since the X-axis travels down the nominal ¼ chord, the differences in the intercepts is a direct measure of the out-of-plane elastic bending in Z. The differences in slope angle are a measure of the induced elastic twist, which will be shown later.

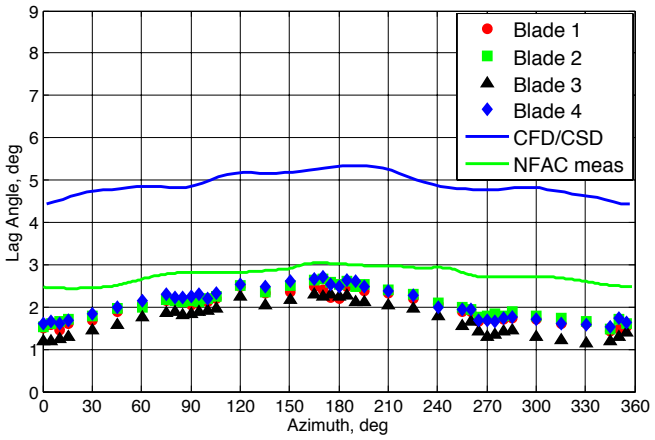

a. Blade 1-4 lag angle and CFD/CSD predictions vs. azimuth.

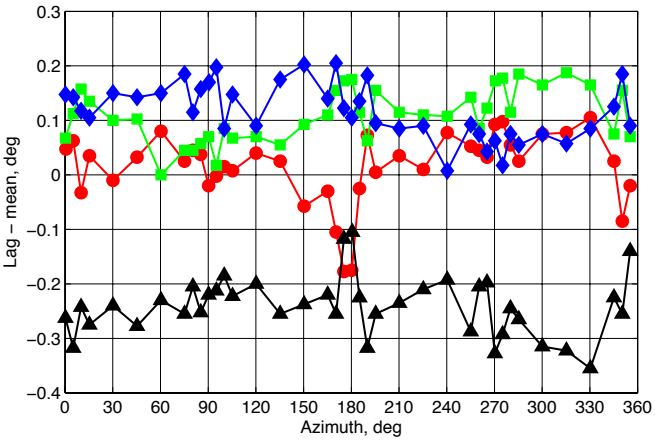

b. Blade-to-blade differences in lag angle vs. azimuth.

Figure 16. Blade lag angle vs. azimuth, $\mu = 0.30$, $C_T/\sigma = 0.10$, $M_{tip} = 0.65$.

The out-of-plane elastic bending at the blade tip (r/R = 0.97) is plotted versus azimuth in Fig. 17. The elastic bending at r/R = 0.97 varies from -15 inches (downward bending) at $\psi = 150°$ to seven inches (upward bending) at $\psi = 265°$ (Fig. 17a). The elastic bending is similar for all blades and agrees well with CFD/CSD. As mentioned above in the Measurement Process Uncertainty Considerations section, the experimental results for elastic bending and twist are expected to be influenced by the bias error in the transformation from measured to the reference geometry.

To emphasize blade-to-blade differences the experimental data is re-plotted in Fig. 17b with the four-blade mean value at each azimuth subtracted. When data was not available from all four blades, i.e. blade 3 and 4 at 225° azimuth, linear interpolation was used to compute the mean value at that azimuth angle. No azimuthally systematic differences are discernable in this data. The mean bending over 360° for blades 1 and 3 (the pressure and strain gage blades) differ by 0.67 inch. The non-instrumented blades, blades 2 and 4, show negligible difference. Fig. 17c shows the elastic bending standard deviation for all four blades near the blade tip, r/R = 0.97. It can be seen from this data that

the elastic bending of the blades at a given azimuth are not significantly different.

At each radial station, the slope angle of the reference geometry is subtracted from the slope angle of the measured blade to determine elastic twist. Thus a positive value of elastic twist represents nose-up induced twist. The built-in twist, which is present in both the reference and transformed measured data set, is automatically compensated by this method. The induced twist of the lower surface targets measured in this manner is assumed to follow the induced elastic twist of the displaced blade chord line.

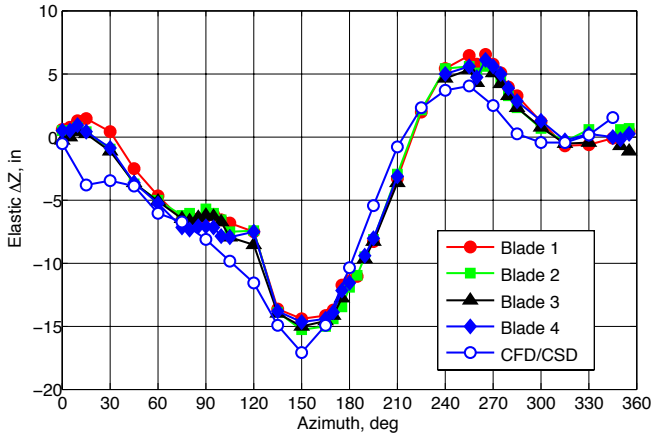

a. Elastic bending with CFD/CSD comparison.

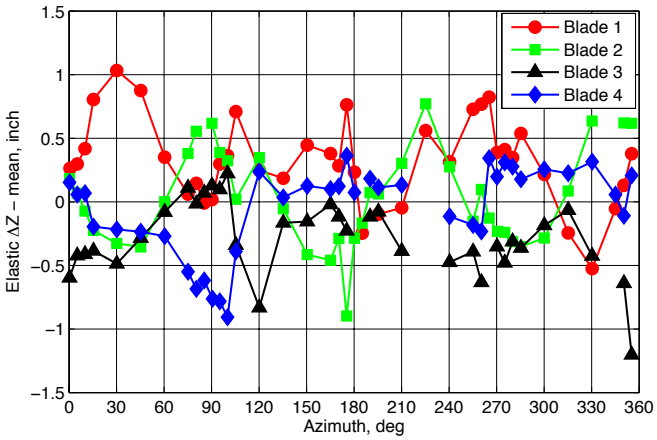

b. Blade-to-blade differences in elastic bending.

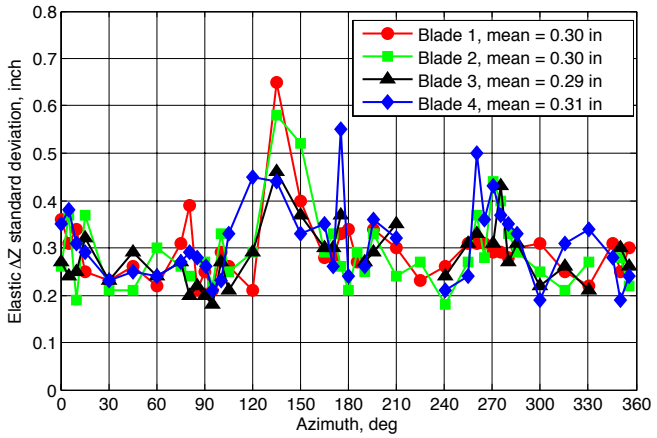

c. Standard deviation of elastic bending.

Figure 17. Blades 1-4 elastic bending of the blade tip, r/R = 0.97, $\mu = 0.30$, $C_T/\sigma = 0.10$, $M_{tip} = 0.65$.

The elastic twist near the blade tip (r/R = 0.97) is plotted versus azimuth in Fig. 18. The elastic twist at r/R = 0.97

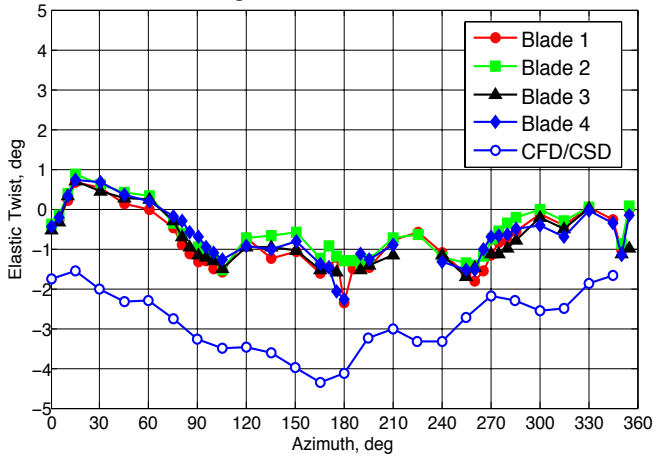

a. Elastic twist with CFD/CSD comparison.

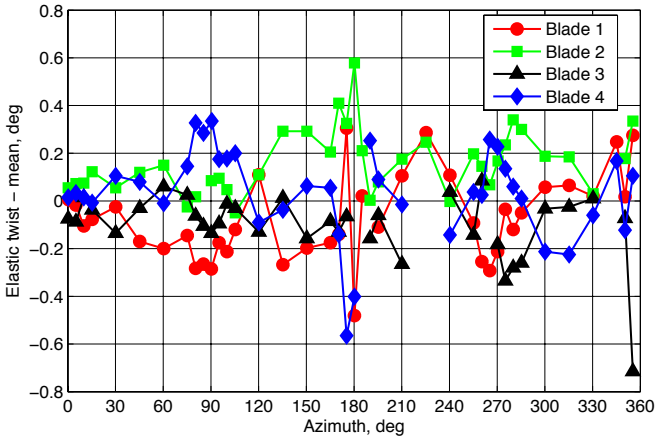

b. Blade-to-blade differences in elastic twist.

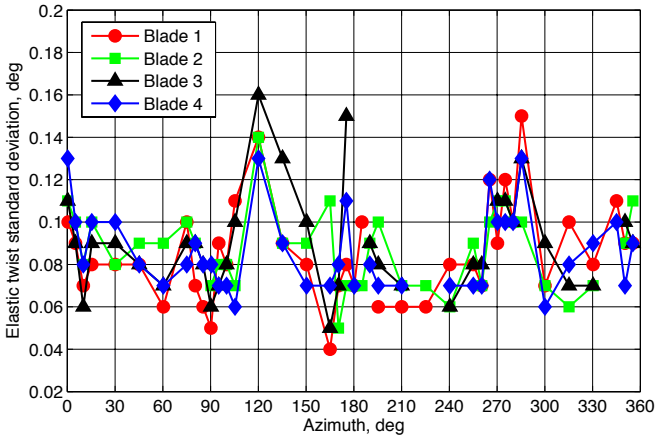

c. Standard deviation of elastic twist.

Figure 18. Blades 1-4 elastic twist at the blade tip, r/R = 0.97, $\mu = 0.30$, $C_T/\sigma = 0.10$, $M_{tip} = 0.65$.

varies from -2° at ψ= 180° to 1° at ψ = 15° (Fig. 18a). The elastic twist is similar for all blades. The CFD/CSD analysis shows a similar trend, but with an offset of 2° from the experimental.

To emphasize blade-to-blade differences the experimental data is re-plotted in Fig. 18b with the four-blade mean value at each azimuth subtracted out. No azimuthally systematic differences are discernible in this data. Figure 18c presents the standard deviation of the elastic twist for all four blades near the blade tip, r/R = 0.97. It can be seen from this data that the elastic twist of the blades at a given azimuth are not significantly different.

Figure 19 presents examples of experimental and corresponding computational out-of-plane elastic bending versus r/R at 0°, 150° and 255° azimuth angles. Each figure contains data from 60 consecutive rotor revolutions of Blade 2 at the nominal ¼-chord location 5.19 inches from the leading edge (neglecting the slight change in the ¼ chord that occurs on the blade due to a change in sectional airfoil shape). Predicted data is presented using two different methods for extracting the elastic deformations: (1) by removing the exact rigid body motions (RBM) as indicated by flap hinge deflection and (2) by removing an estimate of the rigid body motions as computed by a best fit line through the predicted data at 0.20, 0.25, 0.30, and 0.35 r/R. The former method is the most accurate and yields only the elastic deformation predicted by the structural model. The latter method simulates (with predicted data only) how the coordinate transformations are computed for the measured data using values from the first four radial stations. For each azimuth, approximately two inches of vertical separation exist between the two predicted curves at the rotor tip. This difference is the result of just a 0.36° difference in rigid body flapping.

The elastic rotor deformations show rev-to-rev variations that are similar in magnitude. The maximum instantaneous elastic bending is less than one-inch over the span of the blade at 0° azimuth with a mean value over 60 revolutions of 0.5 inches near the blade tip. At an azimuth of 150° the elastic deformation at the blade tip (r/R = 0.97) is 15 inches in the downward direction. At an azimuth of 255° the elastic deformation at the blade tip is 5.5 inches in the upward direction.

In all cases, the measured data is bracketed by the two predicted curves. This inspires confidence in both the predictions and measurements but suggests that further work might find a technique that can more accurately remove the rigid body motions from the measured data.

The standard deviations of the ¼-chord elastic bending for 60 revolutions versus r/R are shown in Fig. 20. Coordinate transformation solves at each revolution are made to effectively remove rev-to-rev variations in pitch, flap, and lag angle that could overwhelm the much smaller

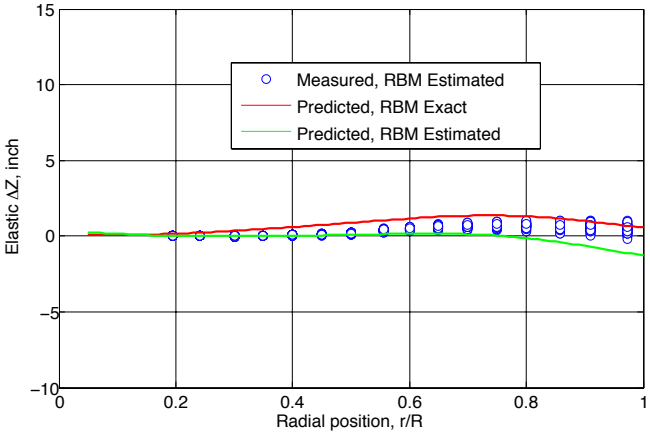

a. Elastic bending, blade 2 at ψ = 0°.

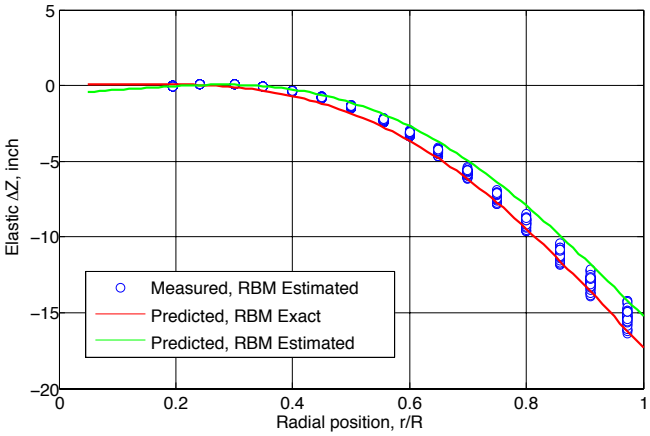

b. Elastic bending, blade 2 at ψ = 150°.

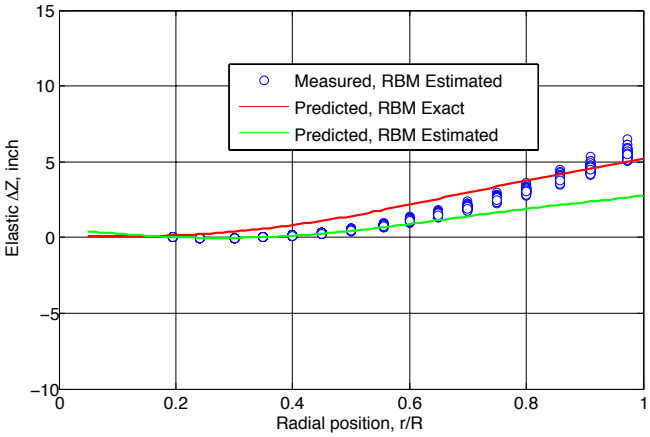

c. Elastic bending, blade 2 at ψ = 255°.

Figure 19. Blade 2 elastic bending, 60 revolutions, mean, and computed, μ = 0.30, C_T/σ = 0.10, M_{tip} = 0.65.

elastic deformations, particularly inboard. After this removal of rev-to-rev rigid body motion, the outboard elastic oscillations of the blade are still typically 25 to 50 times greater than the inboard portion of the blade for this moderate advance ratio case. Also presented in Fig. 21 are the variations of elastic bending versus revolution at the most inboard blade station, r/R = 0.20, and most outboard blade station, r/R = 0.97, for ψ = 0°, 150° and 255. In Fig. 21

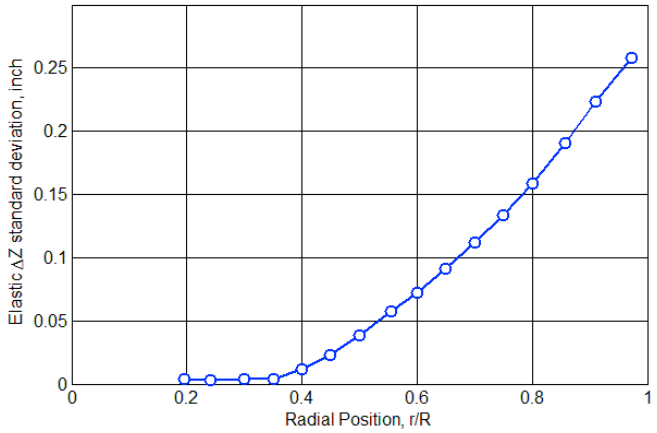

a. Elastic ΔZ standard deviation, blade 2 at ψ = 0°.

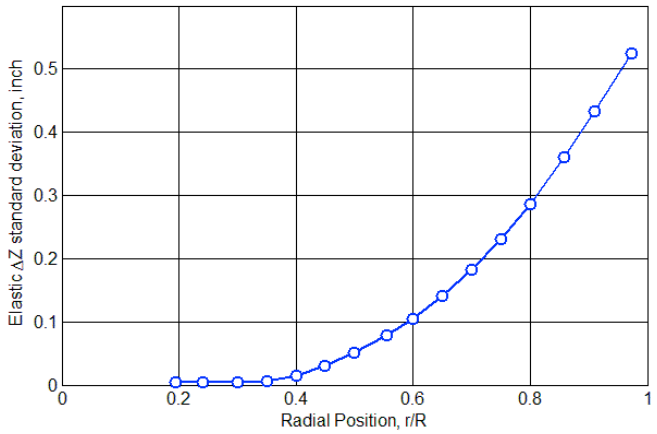

b. Elastic ΔZ standard deviation, blade 2 at ψ = 150°.

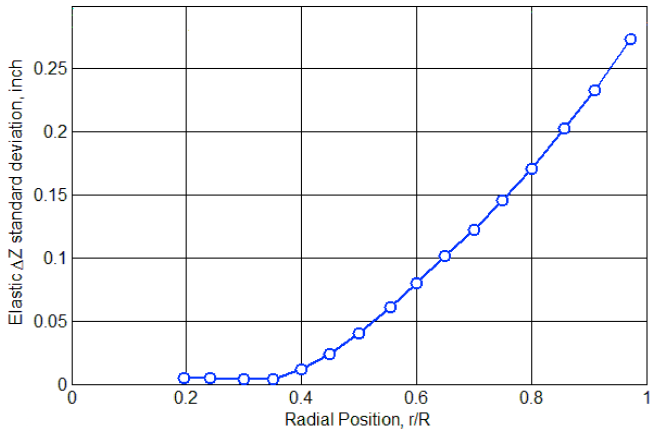

c. Elastic ΔZ standard deviation, blade 2 at ψ = 255°.

Figure 20. Elastic ΔZ standard deviation of ¼-chord elastic bending for 60 revolutions vs. r/R, μ = 0.30, C_T/σ = 0.10, M_{tip} = 0.65.

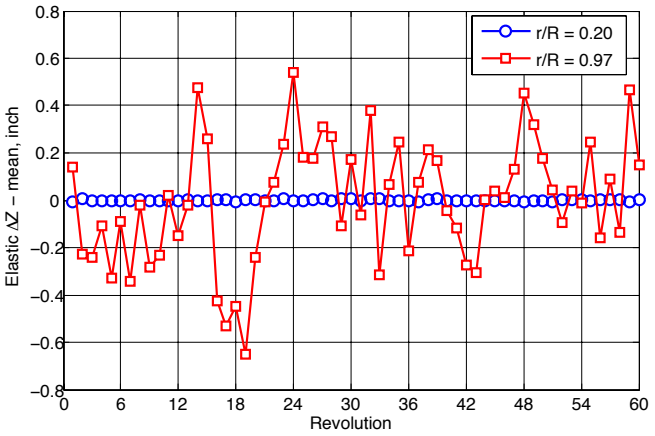

a. Elastic ΔZ variation, blade 2 at ψ = 0°.

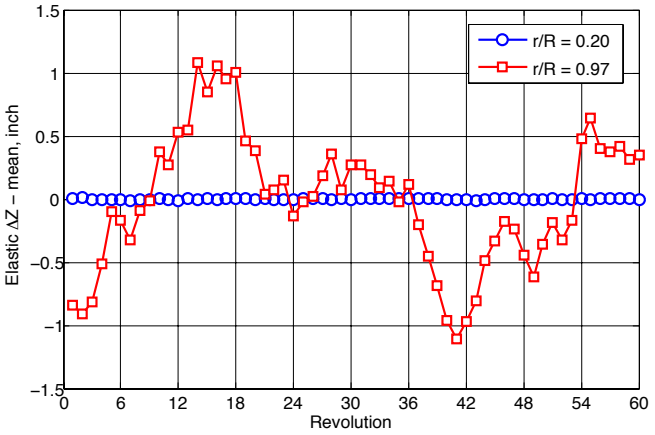

b. Elastic ΔZ variation, blade 2 at ψ = 150°.

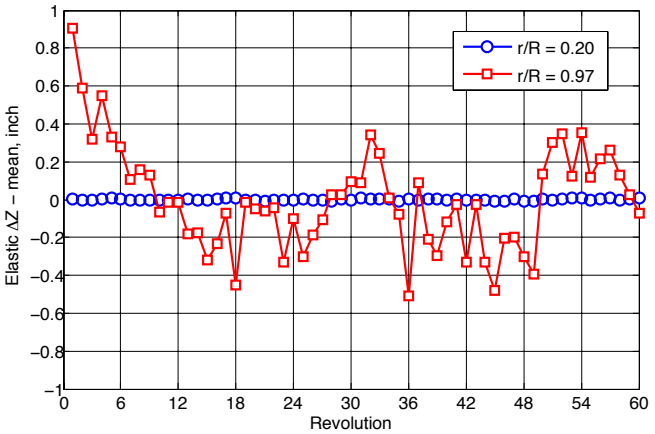

c. Elastic ΔZ variation, blade 2 at ψ = 255°.

Figure 21. Change in ¼ chord elastic bending at r/R=0.20 and r/R = 0.97 vs. revolution, μ = 0.30, C_T/σ = 0.10, M_{tip} = 0.65.

the mean values over the 60 revolutions have been removed to facilitate comparisons of inboard to outboard on the blade. These rev-to-rev variations show (actual) differences in the elastic bending of the outboard portion of the blade relative to the inboard and are not due to scatter in the measurement technique. For Figs. 20 and 21, the measurement precision is much smaller than the symbol size indicates.

Similar to the elastic bending data presented earlier, Fig. 22 represents examples of experimental and computational elastic twist versus r/R at 0°, 150° and 255° azimuth angles. Each azimuth set contains data for 60 consecutive rotor revolutions. Unlike elastic bending, the computed and experimental elastic twist show significant differences. Based on the results of the Measurement Process

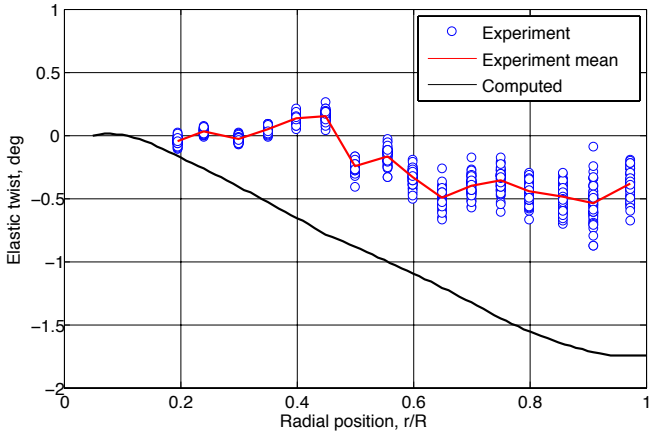

a. Elastic twist, blade 2 at ψ = 0°.

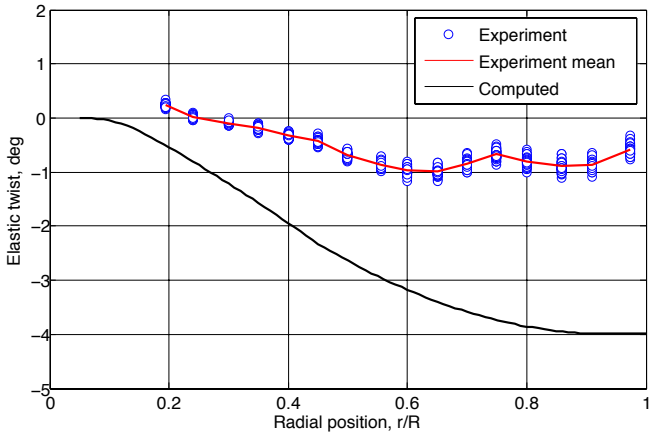

b. Elastic twist, blade 2 at ψ = 150°.

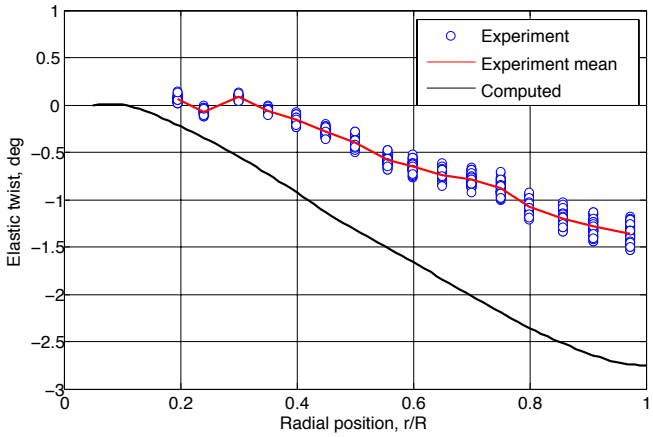

c. Elastic twist, blade 2 at ψ = 255°.

Figure 22. Blade 2 elastic twist, 60 revolutions, mean and computed.

Uncertainty Considerations section, the experimental measurements of elastic twist are expected to underestimate the twist. However, such a large variation between computed and experiment is unexplained at present. Future comparisons with lower advance ratio cases and further study of the differences in the experimental and computational procedures to determine elastic twist should help explain the differences.

The standard deviations for elastic twist versus r/R for the three azimuths are shown in Fig. 23. Like the elastic bending, there is an increase in the elastic twist oscillations as one moves outboard on the blade. However, the ratio of outboard to inboard elastic twist is much less than for elastic bending. As a further example of elastic twist data, Fig. 24 presents the variation in elastic twist about the mean (over the 60 revolutions) for inboard and outboard radial locations

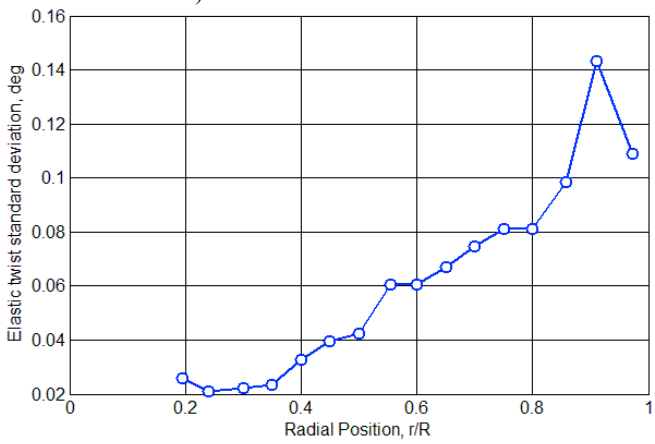

a. Elastic twist variation, blade 2 at ψ = 0°.

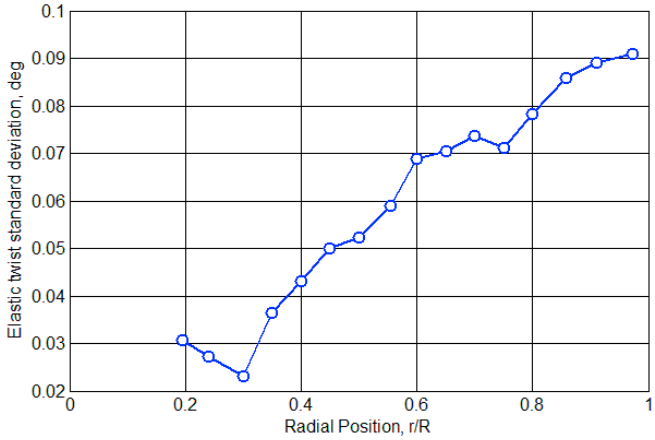

b. Elastic twist variation, blade 2 at ψ = 150°.

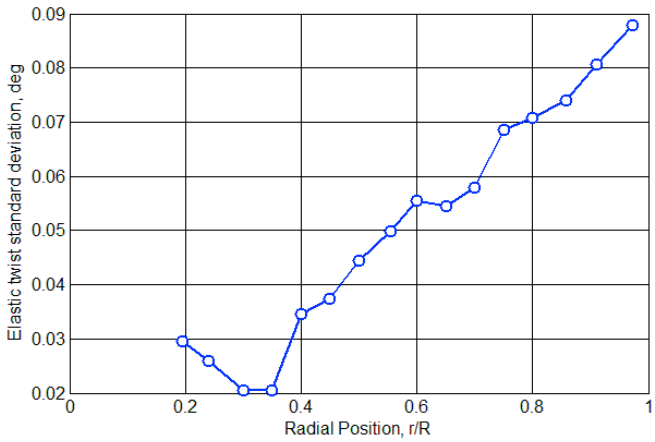

c. Elastic twist variation, blade 2 at ψ = 255°.

Figure 23. Standard deviation of elastic twist for 60 revolutions vs. r/R, μ = 0.30, C_T/σ = 0.10, M_{tip} = 0.65.

versus revolution for the same azimuth angles and test condition as for Figs. 22 and 23. The measurement precision of each data point in Fig. 24 is roughly the size of the symbols. Figure 24 shows slight changes in the elastic twist distribution as a function of revolution that do not correlate in an obvious manner with the changes in elastic bending versus revolution shown in Fig. 21.

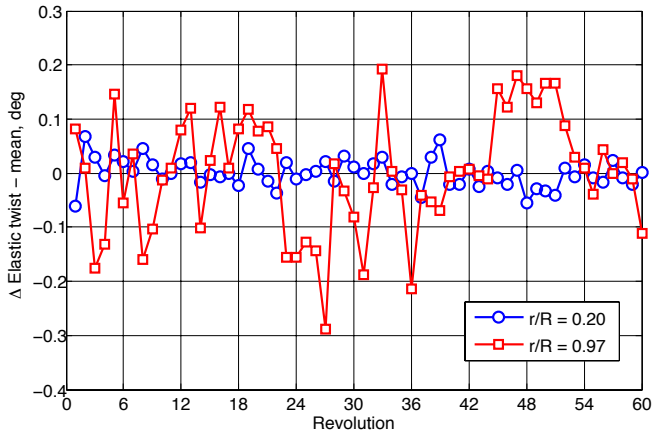

a. Elastic twist variation, blade 2 at ψ = 0°.

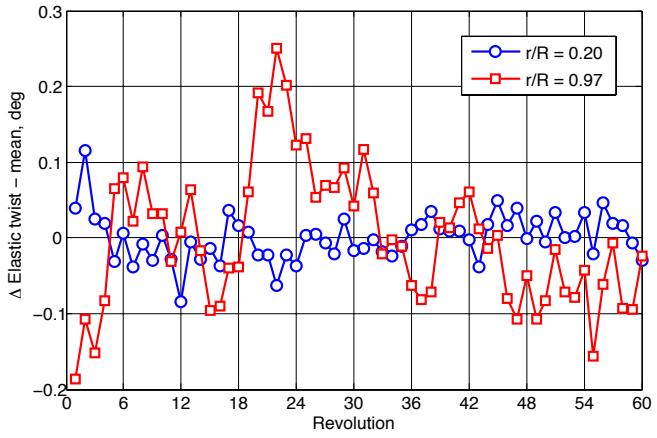

b. Elastic twist variation, blade 2 at ψ = 150°.

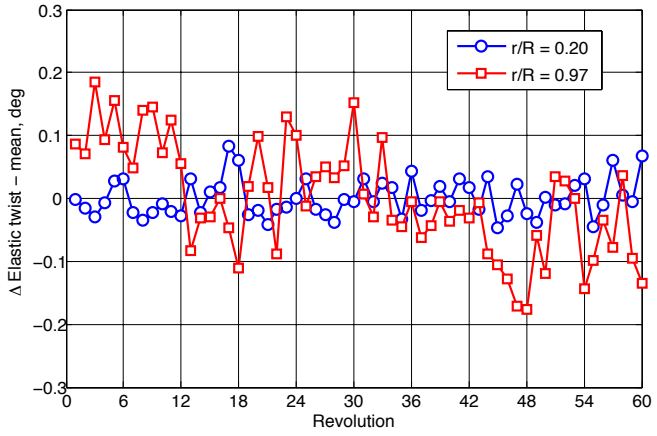

c. Elastic twist variation, blade 2 at ψ = 255°.

Figure 24. Change in elastic twist at r/R=0.20 and r/R = 0.97 about the mean vs. revolution, μ = 0.30, C_T/σ = 0.10, M_{tip} = 0.65.

As a final example, Figs. 25 and 26 show the combined effect of both blade flap and elastic bending for two individual targets, one inboard (r/R = 0.20) and one outboard (r/R = 0.97). These results are derived from 60 image-set averages at each azimuth of the most inboard and outboard targets nearest the quarter chord. The only transformation coefficient applied (other than shaft angle) is the Z-transformation required to align the XYZ blade data at each azimuth to the reference geometry at 0° azimuth. Thus only the Z-component is adjusted from the original shaft-angle-corrected xyz data.

Z-mean at the most inboard (r/R = 0.2) and most outboard (r/R = 0.97) radial stations are shown in Fig. 25a. A mean (azimuthally averaged) flap angle of 4.89° results in an inboard station value near five-inches and an outboard value near 25 inches. As expected the inboard station has a relatively small variation with respect to azimuth position, whereas the station near the blade tip has a range near 25 inches. These results are consistent with the negative elastic bending from approximately 0° to about 220° and the

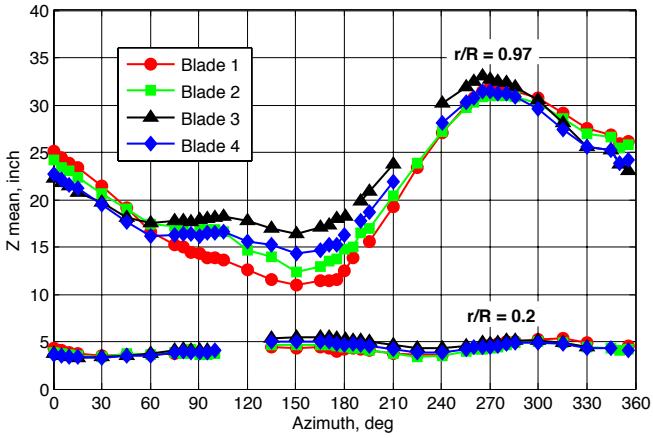

a. Z-mean of target nearest quarter chord vs. azimuth.

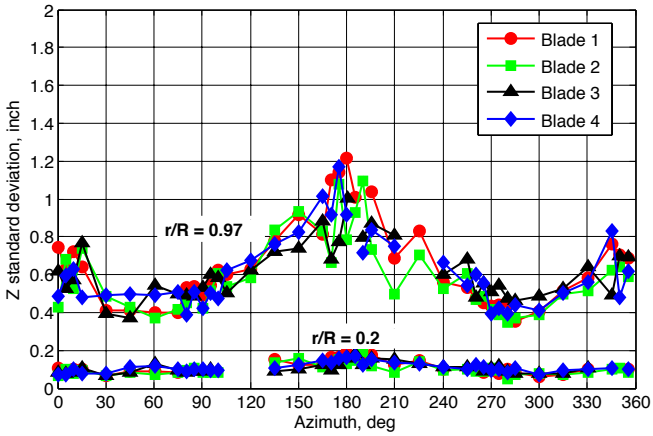

b. Z standard deviation vs. azimuth.

Figure 25. Z mean and standard deviation for blades 1-4, r/R = 0.20 and 0.97, μ = 0.30, C_T/σ = 0.10, M_{tip} = 0.65.

positive elastic bending from 220° to 360° shown in Fig. 15a. Figure 25b shows the Z standard deviation at r/R = 0.20 and 0.97 for each blade. All of the blades behave dynamically in a similar manner when both flapping and elastic bending are included.

The blade-to-blade differences of the Z-coordinate at the inboard station of r/R = 0.20 and the outboard station, r/R = 0.97, are shown in Fig. 26. When data was not available from all four blades, linear interpolation was used to compute the mean (i.e. Fig. 26b, blades 3 and 4 at r/R=0.97 and 220° azimuth). The largest Z-mean variation at both radial stations is between blades 1 and 3, the pressure blade and the strain gage blade. The inboard radial station, Fig. 28a, shows a maximum difference of 1.2 inches at 180° azimuth. Figure 28b, at r/R=0.97, shows a maximum difference of six inches. At these test conditions, the rev-to-rev variations in blade position between 150° and 210° are two to three times those elsewhere in the rotor disk.

Although Figs. 25a and 26b show blade-to-blade differences in Z position at 0.97R approaching six-inches (1.87% of the rotor radius) the blade-to-blade differences in

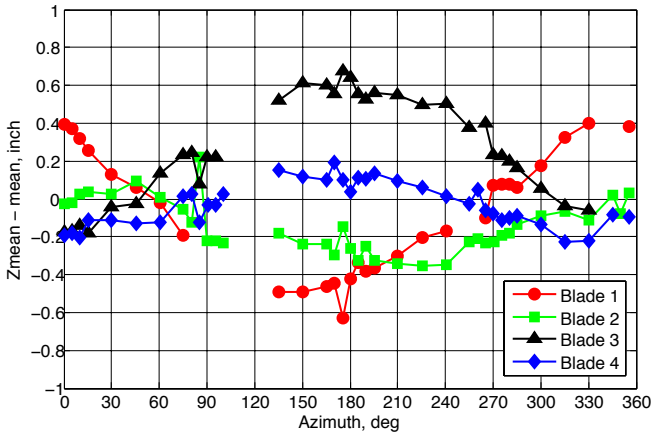

a. Inboard target at r/R = 0.20

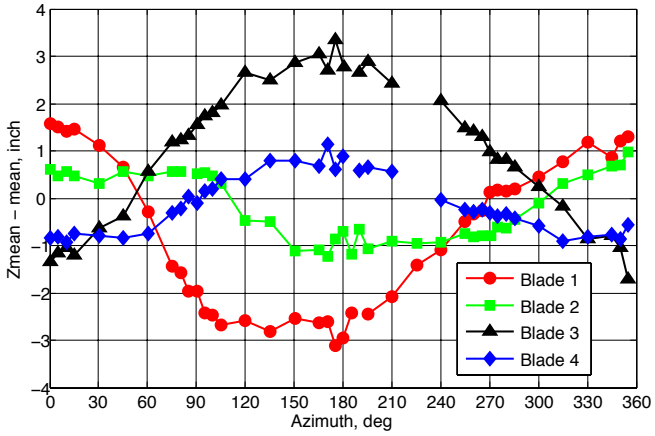

b. Outboard target at r/R = 0.97.

Figure 26. Z-mean blade-to-blade differences of the inboard and outboard leading edge blade tip target, μ = 0.30, C_T/σ = 0.10, M_{tip} = 0.65

elastic bending (Fig. 15) are lower by approximately a factor of five. Therefore the aeroelastic properties of the four blades are not significantly different. Also, when the Airloads rotor is proportionally scaled, under comparable test conditions, the measured Airloads blade-to-blade differences in flapwise deflection are similar in magnitude to those measured during the HART II tests (Ref. 5). This implies that the blade-to-blade variations in the Airloads test in the NFAC are not atypical and are comparable to those observed in another large-scale facility.

Future Work

Efforts continue to improve, validate, and complete the blade displacement measurements for the UH-60A Airloads Wind Tunnel test. Most of the centroids have been obtained for the 27 primary data points with full azimuthal sweeps for the four blades. Centroid inspections for those data points, as well as centroiding for the secondary data points, are underway. The selection of the region of interest around the blade and target identification when less than the full 48 targets are seen as still the most time-consuming part of the image processing. It may be possible to fully automate this portion of the image processing for a limited set of well-behaved targets and images.

Preliminary data reductions have been made for full azimuthal sweeps of all four blades for static, hover, moderate advance ratio (with preliminary results presented above), and slowed rotor high advance ratio test condition. The identification, correction, or removal of outliers in the reduced data is still time-consuming. Comparisons with computational results will continue as part of the validation of both experiment and computations. More detailed investigations of these comparisons will be made with consideration to differences in definitions of what is measured or reported, including the order of the angle rotations, the rotation axis offsets, and other details of both the experimental and computational methods.

Investigations continue with optimization of camera calibration coefficients (preliminary results briefly discussed above). Optimization has the possible advantage that the technique may automate and significantly reduce the amount of time necessary to identify and eliminate outliers in the processed data. Investigations with alternate fish-eye corrections based on equisolid angle projection are underway. With this method, an initial correction is made that removes most of the fish-eye type distortion. The standard 5-parameter distortion correction of radial and asymmetrical lens distortion is then applied to determine the final lens distortion correction. Initial work indicates a slight worsening of intersection standard deviations with the new method compared to the previous method except near the edges of the image plane where the current distortion correction method has either poorer results or fails to converge. A piece-wise interpolation of resection residuals from ceiling reference targets is under consideration to further improve the equisolid fish-eye correction. Another

effort underway that may improve results and significantly reduce the effort and time in outlier removal is the weighting of multiple intersection *XYZ* results by the variance. These new developments will be tested with the static data set to assess any improvements (or detriments) in data reduction procedures as well as in the bias error. A study to review the option of using modal decompositions, as used in the HART II, for the elastic deformation and twist analysis should also be initiated.

CONCLUSIONS

Blade displacement measurements using multi-camera photogrammetry were acquired during the full-scale wind tunnel test of the UH-60A Airloads rotor, conducted in the NFAC 40- by 80-Foot Wind Tunnel. This paper provides an overview of the blade displacement measurement methodology and system development, descriptions of data analysis techniques, uncertainty considerations, and preliminary results covering static and moderate advance ratio test conditions. Initial comparisons with computational analyses are also presented.

The static precision of the photogrammetry technique for pitch, flap, lag, were found from a static azimuthal sweep to be less than 0.01°. However, bias errors over the full range of azimuth can approach 0.4°. The static precision for the important elastic bending and twist were found to be 0.002 inch and 0.012° respectively, with bias errors over the full range of azimuth of 1.2 inch and 0.30° respectively.

Significant bias error in flap is noted for non-zero elastic bending. The error in flap is a direct consequence of the slope in the *Z*-coordinates as a function of radial position on the blade due to elastic bending. Bias errors in the values of flap angle (with a smaller influence from pitch and lag bias errors) lead to a slope error in the transformation to the reference geometry with a corresponding error in elastic bending and twist. The bias error in flap angle causes the experimental results to underestimate the magnitude of the elastic bending and twist. Investigations for a robust method to reduce or eliminate this effect are underway. The error in twist, while extremely sensitive to error between leading and trailing edge targets, is improved somewhat by correlations in error that typically occur between the relatively nearby leading and trailing edge targets. Thus elastic twist and out-of-plane bending (Z) can be determined to an uncertainty significantly less than that indicated by considering the bias errors in Z separately (and uncorrelated). In fact, the uncertainty for elastic deformations can even approach the much smaller values of precision for very closely spaced targets.

Comparisons of experimental and computational values may be complicated since the values of experimental pitch, flap, lag reported here only approximate and are not strictly the usual pitch, flap, lag associated with the blade rotor system. Comparisons of experimental and computational results for a moderate advance ratio forward flight condition show good trend agreements, but show significant mean discrepancies for lag and elastic twist. The experimental values of pitch agree well with the NFAC DAS commanded pitch and NFAC facility measurements using crab-arm and laser sensors. The approximately 2° offset of the experimental and computational results in pitch reflects the adjustment of collective and cyclic to meet specified trim targets necessary for the computational results, thus the offset does not indicate a problem with the experimental data. Reasonable agreement in trend and mean is noted for flap angle. While the trend agreement is good for lag angle, a large offset of nearly 3° is noted for the mean. Trend and mean agreement for elastic bending is reasonable. Trend is reasonable for elastic twist, but there is a mean discrepancy of 2°.

Enhancements to the data reduction procedures are under study in order to reduce the bias errors. These investigations include (1) optimization of camera calibration, (2) alternate fish-eye corrections based on equisolid angle projection, (3) weighting of multiple intersection *XYZ* results by the variance to strengthen the final intersection results, and (4) data processing that does not require the direct transformation of measured blade data to the reference geometry. Optimization has the further advantage that the technique may automate and significantly reduce the amount of time necessary to identify and eliminate outliers in the processed data.

APPENDIX

The following tables present the UH-60A Airloads wind tunnel test conditions with blade displacement primary conditions highlighted in bold.

Parametric Sweep Test Conditions

M_{tip}	α_s	μ	C_T/σ
0.650	-8	0.30	.02 to .12
		0.35	.02 to .11
		0.37	.02 to .11
	-4	**0.15**	**.08**
		0.24	.02 to .126
		0.30	.02 to .118
		0.35	.02 to .11
	0	**0.15**	.04 to .13 **(.08)**
		0.20	.04 to .13
		0.24	.02 to .127 **(0.13)**
		0.30	.02 to .124 **(0.10)**
		0.35	.02 to .11
	4	**0.15**	.06 to .13 **(0.08)**
		0.20	.02 to .12
		0.24	.02 to .12
		0.30	.06 to .08 **(0.08)**
	8	**0.15**	.06 to .12 **(0.08)**
		0.20	.06 to .12
		0.24	.06 to .12
		0.30	**.08**
0.625	0	0.24	.02 to .131
		0.30	.02 to .125
0.675	-8	0.35	.02 to .10
		0.37	.02 to .10
		0.385	.02 to .09

1-g Level Flight Test Conditions

C_L/σ	μ	M_{tip}
0.08	**0.15**, 0.20, 0.24, 0.30, **0.35**, **0.37**, 0.385, **0.40**	**0.650**
0.09	0.15, 0.20, 0.24, 0.30, 0.35, 0.37, 0.385, 0.40	0.650
0.10	0.15, 0.20, 0.24, 0.30, 0.35, 0.37, 0.385	0.650

Flight/DNW Test Simulation Conditions

Test	Test Pt #	M_{tip}	μ	C_T/σ
Flight	**C8424**	**0.638**	**0.30**	**0.087**
	C8525	0.643	0.23	0.077
	C9020	**0.669**	**0.245**	**0.118**
DNW	**11.24**	**0.629**	**0.30**	**0.10**
	13.12	**0.638**	**0.30**	**0.07**
	13.20	**0.637**	**0.15**	**0.07**

Slowed Rotor Test Conditions

M_{tip}	α_s	μ	θ_0
0.650	0	0.30	0, 2, 3, 4, 6, 8, 10
		0.40	0.5, 2, 3, 4, 6, 8
	2	0.30	0, 2, 3, 4, 6, 8, 10
		0.40	0, 2, 3, 4, 6, 8
	4	0.30	0, 2, 3, 4, 6
		0.40	0, 2, 3, 4, 6
0.420	**0**	0.30	0, 2, 3, 4, 6, 8
		0.40	0, 2, 3, 4, 6, 8
		0.50	0, 2, 3, 4, 6, 8
		0.60	**0**, 2, 3, 4, 6, 8
0.260	**0**	0.30	0, 2, 3, 4, 6, 8
		0.40	0, 2, 3, 4, 6, 8
		0.50	0, 2, 3, 4, 6, 8
		0.60	**0**, 2, 3, 4, 6, 8
		0.70	0, 2, 3, 4, 6, 8
		0.80	0, 2, 3, 4, 6, 8
		0.90	0, 2, 3, 4
		1.00	**0**, 1, 2
	2	0.30	2
		0.40	2
		0.50	2
		0.60	**2**
		0.70	2
		0.80	2
		0.90	2
		1.00	**1**
	4	0.30	0, 2, 3, 4, 6, 8
		0.40	0, 2, 3, 4, 6, 8
		0.50	0, 2, 3, 4, 6, 8
		0.60	**0**, 2, 3, 4, 6, 8
		0.70	0, 2, 3, 4, 6, 8
		0.80	0, 2, 3, 4, 6, 8
		0.90	0, 2, 3, 6
		1.00	**0**, 2

PIV Test Conditions

M_{tip}	α_s	μ	C_T/σ	Azimuth delay
0.65	0	0.15	0.08	5, 15, 30, 45, 60, 75, 95, 135, 185, 225, 275, 315
0.65	4	0.15	0.08	5, 15, 30, 45, 60, 75, 95, 135, 185, 225, 275, 315
0.638	-4.82	0.30	0.087	5, 15, 30, 45, 60, 75, 95
0.65	0	0.24	0.07, 0.09	5
0.65	**0**	**0.24**	**0.11**	**5, 15, 30, 45, 60, 75, 95, 185, 275**
0.65	0	0.15	0.07, 0.09, 0.11, 0.12	15
0.65	**-6.9**	**0.35**	**0.08**	**5, 10, 15, 20, 30, 45, 60, 75, 95, 185, 275**

ACKNOWLEDGMENTS

The authors thankfully recognize the efforts and significant contributions made during the planning, development, and implementation of the blade displacement measurements for UH-60A Airloads Wind Tunnel Test. Acknowledgement is made to Thomas Norman, Gloria Yamauchi, Alan Wadcock (NASA Ames), and Gary Fleming (NASA LaRC) for their early involvement with the BD measurement effort. Gary Fleming also developed and provided assistance with the rotor azimuth synchronization program (RASP). Edward Massey (Jacobs Technology-NASA LaRC) is acknowledged for his modifications to the WingViewer image acquisition software to accommodate special requirements for rotor testing. Further acknowledgement is extended to Susan Gorton, Luther Jenkins and Odilyn Santamaria-Luck (NASA LaRC) for program leadership and to Harriett Dismond, Benny Lunsford, Kelvin Santiago, Felecia Berry, Kristina Chapman, Lisa Le Vie (NASA LaRC), Larry Meyn, Eduardo Solis, Charles Rogers, Michael Henderson, Benny Cheung, and Dan Christensen (NASA Ames), along with the entire NFAC test team for their strong support of the BD effort.

In addition Thomas Jones (NASA LaRC) is acknowledged for technical advice in camera self-calibration and for calibrations of four of the cameras. Professors Stuart Robson (University College London) and Mark Shortis (RMIT University, Melbourne, Australia) are acknowledged for consultation on the distortion of fish-eye lenses and alternate methods of lens correction.

Finally, we wish to acknowledge and thank the recent retiree Larry Olson for his dedication, hard work, and innovations with the Blade Displacement Measurement effort. We wish him the very best in his retirement.

REFERENCES

1. Norman, T. R., Shinoda, P., Peterson, R. L. and Datta, A., "Full-Scale Wind Tunnel Test of the UH-60A Airloads Rotor," American Helicopter Society 67th Annual Forum, Virginia Beach, VA, May 2011.

2. Kufeld, R. M., Balough, D. L., Cross, J. L., Studebaker, K. F., Jennison, C. D. and Bousman, W. G., "Flight Testing of the UH-60A Airloads Aircraft," American Helicopter Society 50th Annual Forum, Washington D.C., May 1994.

3. Jenkins, L. N., Barrows, D. A., Cheung, B. K., Lau, B. H., Okojie, R. S., Wadcock, A. J., Watkins, A. N. and Yao, C. S., "Chapter 5 – Experimental Capabilities, A Status of NASA Rotorcraft Research", edited by Gloria K. Yamauchi and Larry A. Young, NASA TP-2009-215369, September 2009.

4. Bosnyakov, S., Bykov, A., Coulech, V., Fonov, S., Morozov, A., Moskalik V., Moskalik L., Mosharov, V., Orlov A., Radchenko, V. and Tarassov, N., "Blade Deformation and PSP Measurements on the Large Scale Rotor by Videometric System," ICIASF 1997 – 17th International Congress on Instrumentation in Aerospace Simulation Facilities, Pacific Grove, Calif., Sept. 1997.

5. Schneider, O. and Van der Wall, B. G., "Final Analysis of HART II Blade Deflection Measurement," 29th European Rotorcraft Forum, Friedrichshafen, Germany, September 16-18, 2003.

6. Olson, L. E., Barrows, D. A., Abrego, A. I. and Burner, A. W., "Blade Deflection Measurements of a Full-Scale UH-60A Rotor System," 2010 AHS Specialists' Conference on Aeromechanics, San Francisco, CA, January 20-22, 2010.

7. Norman, T. R., Shinoda, P. M., Kitaplioglu, S. A., Jacklin, S. A. and Sheikman, A., "Low-Speed Wind Tunnel Investigation of a Full-Scale UH-60 Rotor System," American Helicopter Society 58th Annual Forum, Montreal, Canada, June 2002.

8. Luhmann, T., Robson, S., Kyle, S., and Harley, I., *Close Range Photogrammetry: Principles, Techniques and Applications*, John Wiley & Sons, 2006.

9. Burner, A. W. and Liu, T., Videogrammetric Model Deformation Measurement Technique. AIAA J. of Aircraft, vol. 28, no. 4, July-August, 2001, pp. 745-754.

10. Geodetic Systems, Inc., http://www.geodetic.com/.

11. Barrows, D. A., Burner, A. W., Olson, L. E., and Abrego, A. I., "Blade Displacement Measurements of the Full-Scale UH-60A Airloads Rotor", 2011 AIAA Applied Aerodynamics Conference, Honolulu, Hi, June 27-30, 2011.

12. Fleming, G. A., "RASP: Rotor Azimuth Synchronization Program (RASP) User's Guide, Version 1.3", NASA Langley Research Center, February 6, 2008.

13. Amer, T. R. and Goad, W. K., "WingViewer: Data-Acquisition Software for PSP/TSP Wind Tunnel Cameras", NASA Langley Research Center, LAR-16474-1, October 2005.

14. Liu, T. and Burner, A. W., "Photogrammetry Toolbox User's Guide," Western Michigan University in Kalamazoo, MI, May 2007.

15. Romander, E., Norman, T. R. and Chang, I. C.. "Correlating CFD Simulation With Wind Tunnel Test for the Full-Scale UH-60A Airloads Rotor," American

Helicopter Society 67th Annual Forum, Virginia Beach, VA, May 3 -5, 2011.

16. Kufeld, R. M. and Bousman, W. G., "UH-60A Airloads Program Azimuth Reference Correction," Technical Note, American Helicopter Society J. April 2005, pp. 211-213.

17. Ahmad, J. and Biedron, R. T., "Code-to-Code Comparison of CFD/CSD Simulation for a Helicopter Rotor in Forward Flight," 2011 AIAA Applied Aerodynamics Conference, Honolulu, Hi, June 27-30, 2011.

18. Tung, C., Caradonna, F. X. and Johnson, W., "The Prediction of Transonic Flows on an Advancing Rotor," American Helicopter Society 40th Annual Forum, Arlington, VA, May 16-18, 1984.

19. Potsdam, M., Yeo, H. and Johnson, W., "Rotor Airloads Prediction Using Loose Aerodynamic/ Structural Coupling," Journal of Aircraft, Vol. 43, No. 3, May-June 2006.